

Enhancing dust aerosols monitoring capabilities across North Africa and the Middle East using the A-Train satellite constellation

Anna Moustaka^{1,2,3}, Nikolaos Siomos⁴, Stelios Kazadzis², Emmanouil Proestakis³, Kalliopi Artemis Voudouri^{3,1}, Anton Lopatin⁵, Oleg Dubovik⁶, Kleareti Tourpali¹, Christos Zerefos^{7,8,9,10}, Vassilis Amiridis³, and Antonis Gkikas^{7,3}

¹ Department of Physics, Aristotle University of Thessaloniki, 54124, Greece

² Physicalisch Meteorologisches Observatorium, World Radiation Center, Davos, 7260, Switzerland

³ Institute for Astronomy, Astrophysics, Space Applications and Remote Sensing, National Observatory of Athens, Athens, 11810, Greece

⁴ Chair of Experimental Meteorology, Faculty of Physics, Ludwig-Maximilians-Universität München, 80539, Germany

⁵ GRASP SAS, Lille, 59000, France

⁶ Laboratoire d'Optique Atmosphérique, CNRS/Université de Lille, Villeneuve-d'Ascq, 59650, France

⁷ Research Centre for Atmospheric Physics and Climatology, Academy of Athens, Athens, 11521, Greece

⁸ Biomedical Research Foundation, Academy of Athens, Athens, 11527, Greece

⁹ Navarino Environmental Observatory (N.E.O.), Messinia, 24001, Greece

¹⁰ Mariolopoulos-Kanaginis Foundation for the Environmental Sciences, Athens, 11251, Greece

Correspondence to: Anna Moustaka (anna.moustaka@pmodwrc.ch)

Abstract. North Africa and the Middle East encompass the most active dust sources on the planet. Due to the limited availability of ground-based aerosol observations across the deserts, spaceborne retrievals represent the most reliable source of information for monitoring dust particles over these vast areas. In the current study, we present a synergistic approach incorporating aerosol retrievals acquired by active (CALIOP) and passive (POLDER-3, MODIS) instruments mounted on satellites of the A-Train constellation. Our main objective is to dynamically (in terms of space and time) estimate the dust lidar ratio (LR) at 532 nm throughout a 12-year period (2006-2017) by collocating columnar aerosol optical depth observations (POLDER-3/GRASP, MIDAS) and vertically resolved dust aerosol profiles obtained by CALIPSO. According to our findings, the derived dust LRs reveal a clear spatial variability. The highest LRs are found over major Saharan source regions such as the Bodélé Depression and the Libyan Desert, while moderate to low values dominate the Arabian Peninsula. Enhanced values also appear across Central Asia, particularly over the Karakum and Kyzylkum deserts. The corresponding uncertainty fields demonstrate that LR estimates are most robust over regions with a larger number of dust cases, whereas higher uncertainties occur along transition zones—such as the Sahel and parts of Central Asia—where dust mixing or aerosol-type misclassification increases retrieval variability. A key objective of this work is to establish a robust methodology for deriving aerosol-specified LRs using synergies between active and passive observations. Although focused here on dust over North Africa and the Middle East, the same framework can be readily applied to other CALIPSO aerosol subtypes—such as marine, polluted dust, or smoke—when implemented over regions where these aerosol types predominate. The advent of the EarthCARE satellite mission, along with the incorporation of new aerosol models into the forthcoming CALIPSO Version 5 aerosol retrieval

algorithm, will serve as a reference for our calculations. In this context, our findings also highlight that a synergy of multisensor aerosol products with modelling tools can enhance the spatiotemporal representation of aerosol properties, such as the LR, further improving retrieval utility.

40 **1 Introduction**

Dust aerosols represent a significant component of the global aerosol burden, profoundly influencing climate and various environmental processes (Zender et al., 2004; Textor et al. 2006; Mahowald et al., 2014; Gkikas et al., 2021; 2022; Logothetis et al., 2021; González-Romero et al., 2023; Castellanos et al., 2024). The most prominent dust sources are located in arid and semi-arid regions, where the prevailing meteorological conditions and the soil characteristics facilitate the mobilization of dust
45 particles (Ginoux et al., 2012; Prospero et al., 2013; Huang et al., 2014; Chen et al., 2018). North Africa features some of the most active dust sources worldwide. The Bodélé Depression in the northern Chad Basin, is recognized as the most prolific single source of mineral dust globally (Warren et al., 2007; Ginoux et al. 2012; Kok et al., 2021), with substantial emissions also emanating from the western Sahara, the eastern Libyan Desert, and the Nubian Desert (Sudan and Egypt) (Engelstaedter et al. 2007). The spatial extent and intensity of these sources vary significantly depending on the prevailing winds and surface
50 conditions (Mbourou et al., 1997; Schepanski, 2018; Tindan et al., 2023).

The Arabian Peninsula also serves as a major source region for mineral dust aerosols. The Rub' al Khali desert, one of the largest continuous sand seas in the world, contributes substantially to regional and global dust loading (Jish Prakash et al. 2015). Other significant sources include alluvial plains within the Tigris-Euphrates river system and sandy deserts across the region (Pease et al., 1998; Hamidi et al., 2013). Dust emissions across the Arabian Peninsula show strong seasonality,
55 influenced by the prevailing winds and the availability of loose, erodible material on the surface (Yu et al., 2013; 2015; Solmon et al. 2015). The transport of dust from this region significantly affects the atmospheric composition and radiative balance of the Middle East, western parts of Asia and the Eastern Mediterranean (Jish Prakash et al., 2015). Desert regions in Central Asia contribute to global dust emissions, albeit typically at lower intensities than those in North Africa and the Arabian Peninsula (Xiong et al., 2020). Among these, the Karakum Desert (Turkmenistan) and the Kyzylkum Desert (spanning
60 Uzbekistan and Kazakhstan) stand out as smaller yet significant sources of regional dust loading (Li and Sokolik, 2018). These deserts share similar arid characteristics, but their dust production and transport are influenced by unique geographical factors and meteorological conditions (Banks et al., 2022).

The complex nature of mineral dust aerosols, in terms of particle sizes, shapes, and compositions (Castellanos et al., 2024), leads to significant challenges for accurate remote sensing and modeling, necessitating the deployment of advanced
65 observational techniques. Ground-based measurements employing passive and active remote sensing techniques have provided invaluable long-term data on aerosol intensive and extensive properties (Groß et al., 2011; 2015; Burton et al., 2012; Baars, et al., 2016; Benkhalifa et al., 2017; Haarig et al., 2017a; 2017b; 2022; Ningombam et al. 2019; Hofer et al., 2020; Raptis et al. 2020; Yu et al., 2022;). Spaceborne observations from passive sensors, such as those from the Moderate Resolution Imaging

Spectroradiometer (MODIS) onboard Terra and Aqua satellites, have delivered multi-year records of columnar aerosol optical depth (AOD) with near-global coverage since 2000 (Luo et al., 2014; Mao et al., 2014; Gupta et al., 2020; Gkikas et al., 2021; Kang et al., 2023). The recently developed MODIS Dust Aerosol (MIDAS) dataset (Gkikas et al., 2021; 2022) further refines dust-specific AOD by combining MODIS-Aqua quality-assured AOD retrievals with Modern-Era Retrospective analysis for Research and Applications version 2 (MERRA-2; Gelaro et al., 2017) reanalysis dust fraction ratios (in optical terms), offering a high-resolution record of daily dust optical depth (DOD) on a global scale, spanning from 2003 to 2017 (Gkikas et al., 2021). Additionally, the multi-angle, multi-spectral polarimetric (MAP) measurements have been providing comprehensive data on aerosol particle size, shape, and refractive index, enabling detailed characterization of aerosols' properties and interactions within the atmosphere since the mid-1990s (Hansen et al., 1995; Mishchenko and Travis, 1997a; 1997b). Polarimetric measurements from the Polarization and Directionality of the Earth's Reflectances (POLDER-3) on the PARASOL platform exemplify the contributions of MAP technology to aerosol science. When combined with the Generalized Retrieval of Atmosphere (GRASP), the linearly polarized and total radiances from POLDER-3 sensor enables the retrieval of detailed aerosol properties, such as particle size distribution, complex refractive indices, and sphericity. Furthermore, POLDER-3/GRASP achieves high-quality AOD (Dubovik et al., 2011; Li et al., 2019; Chen et al., 2020; Zhang et al., 2021), validated effectively against AERONET stations (Chen et al., 2020; Zhang et al., 2021).

Along with space-borne passive sensors measuring the reflectance at the top of the atmosphere (TOA), active remote sensing techniques, offer superior capabilities for resolving the vertical distribution of aerosols throughout the atmosphere. From June 2006 to August 2023, the Cloud-Aerosol Lidar with Orthogonal Polarization (CALIOP) instrument onboard the Cloud-Aerosol Lidar and Infrared Pathfinder Satellite Observation (CALIPSO) satellite provided vertically resolved aerosol retrievals, both day and night, at high spatial and temporal resolutions, regardless the underlying surface type (Winker et al., 2010). Among the prediscussed limitations of the CALIOP's elastic lidar in a number of previous studies (Winker et al., 2009; Ma et al., 2013; Kim et al., 2018; Gui et al., 2022; Haarig et al., 2018; Li et al., 2022; Moustaka et al., 2024), the accuracy of CALIPSO's AOD retrievals is highly contingent on the predetermined extinction-to-backscatter ratio, a key parameter defined as lidar ratio (LR), which varies significantly depending on aerosol types. This dependency can lead to inaccuracies, especially if the LR assigned to an aerosol type does not adequately reflect its true microphysical characteristics. Schuster et al. (2012) indicated that CALIPSO's AOD is often underestimated by approximately 13% when compared to AERONET. This underestimation is attributed to both aerosol misclassification and inaccuracies in the modeled microphysics for certain aerosol types, such as polluted dust or smoke. Additionally, CALIOP's ability to measure particle linear depolarization at 532 nm has provided great insights into identifying non-spherical mineral dust particles (Burton et al., 2013).

Specifically, for the non-spherical dust particles, the study from Amiridis et al. (2013) has shown that the increase of dust LR over the Sahara leads to better accuracy of AOD by reducing the observed discrepancies compared to MODIS and AERONET. According to a more recent study from Moustaka et al. (2024), the authors used the DeLiAn database (Depolarization ratio, Lidar ratio, and Ångström exponent database; Floutsi et al., 2023), a collection of state-of-the-art ground-based lidar observations acquired in areas characterized by different aerosol conditions, in order to estimate the effect of an updated

aerosol-speciated LR on AOD and subsequently to the direct radiative effects (DREs) across the North Africa, Middle East and Europe domain (NAMEE). Using DeLiAn-derived LRs reduced differences between CALIPSO and AERONET observations in dust-dominated regions, leading to more reliable DRE estimates. Under moderate-to-high aerosol loads, this approach enhanced the calculated surface cooling and atmospheric warming by up to 35%. These findings along with those of past relevant studies (Omar et al., 2013; Konsta et al., 2018) underscore the importance of accurately determining the dust LR, across major desert regions over the globe. The adaptation of a more ‘realistic’ dust LR can enhance the accuracy of elastic lidar-derived AOD estimates. In addition to the LR, other properties of dust, including its emission processes, mineralogical composition, and morphology, are crucial for assessing its climatic role, as they influence key optical characteristics like DOD, single scattering albedo (SSA), and refractive index, which are essential inputs for radiative transfer models (RTMs). A deeper understanding of these properties allows for a more accurate representation of dust microphysical characteristics and radiative effects, ultimately improving climate predictions and reducing uncertainties in dust-related DREs (Kok et al., 2017; 2023). Our study focuses on improving dust aerosol monitoring across North Africa and the Middle East by refining dust LR estimates at 532 nm via a synergistic approach between active and passive sensors of the A-Train satellite constellation. Based on the CALIPSO aerosol classification scheme, which uses accurate depolarization measurements of the CALIOP lidar to detect non-spherical dust layers, we focus on dust cases. We aim to adjust the dust LR so that the CALIOP DOD at 532 nm matches the coincident columnar observations from the MIDAS (from 2007 to 2017) and POLDER-3/GRASP (from 2006 to 2009) datasets (Section 2). Section 3 provides the full methodological framework, including the definition of dust cases, the multisensor matchup strategy, the estimation and propagation of DOD uncertainties within the A-Train constellation, and the derivation of the dust LR together with its associated uncertainties. In Section 4, we present the geographical distribution of dust LR on an annual and seasonal basis, along with the associated uncertainties. Finally, Section 5 summarizes the main findings and discusses future aspects of the work, including a summary table of regional dust LR estimates that can serve as a practical reference for subsequent studies.

125 **2 Data sets**

2.1 CALIOP-CALIPSO Spaceborne Retrievals

From April 2006 to August 2023, the Cloud-Aerosol Lidar with Orthogonal Polarization (CALIOP) on the Cloud-Aerosol Lidar and Infrared Pathfinder Satellite Observations (CALIPSO) satellite has significantly enhanced our understanding of aerosol and cloud interactions and their roles in the climate system (Winker et al., 2009). CALIOP operates as a dual-wavelength backscatter (532 and 1064 nm) and single-wavelength polarization (532 nm) lidar system. The horizontal averaging and the vertical resolution of the system varies depending on both the altitude and the wavelength. (Winker et al., 2009). This system aids in distinguishing aerosols from clouds and differentiating between fine and coarse-mode aerosol layers, while its depolarization signal is essential for distinguishing between spherical particles (e.g., marine particles, liquid cloud

droplets) and non-spherical particles (e.g., dust, ice cloud particles) within the atmosphere (McGill et al., 2007; Hu et al., 2009; Omar et al., 2009; Burton et al., 2012; 2013; Kim et al., 2018).

The latest version 4.5 (V4.5) of the CALIOP level 2 (L2) aerosol classification product, besides the more comprehensive and accurate definitions of stratospheric particles (Tackett et al., 2023), preserves the same rationality with the previous V4 versions for the tropospheric aerosol layers, using layer-integrated values of depolarization and attenuated backscatter from L1 data, along with geographical location, surface type, and layer altitude information, to assign distinct aerosol types (Kim et al., 2018). The CALIPSO algorithm classifies tropospheric aerosols into seven categories: "marine," "dust," "polluted continental/smoke," "clean continental," "polluted dust," "elevated smoke," and "dusty marine." Dust is one of the most well-characterized subtypes (Burton et al., 2013), thanks to CALIOP's accurate depolarization measurements, which enable the detection of non-spherical dust layers. Critical quality filters are applied during CALIOP-CALIPSO data processing to minimize errors in layer detection, classification, and extinction retrieval, as well as biases from negative signal anomalies. Cloud contamination is also mitigated using the cloud aerosol discrimination (CAD) algorithm and by applying misclassified cirrus fringe filters (Marinou et al., 2017; Proestakis et al., 2018; Tackett et al., 2018).

In the present study, based on the CALIPSO aerosol subtype product, we identify dust scenes during daytime satellite orbits and we exploit quality-assured (QA) vertical profiles of the extinction coefficient at 532 nm, including the corresponding uncertainty estimates, sourced from the LIVAS (Lidar climatology of Vertical Aerosol Structure) database (Amiridis et al., 2015), for the computation of the columnar dust optical depth (DOD) and its relative uncertainty, over a 12-year period (June 2006 to December 2017). LIVAS is a comprehensive 3-D multi-wavelength database that provides global aerosol and cloud optical properties based on CALIPSO observations at 532 and 1064 nm with a resolution of $1^\circ \times 1^\circ$. For the LIVAS development, the ESA-CALIPSO dataset (Wandinger et al., 2011), the EARLINET (The EARLINET publishing group 2000–2010) and AERONET products (Holben et al., 1998; 2001), along with aerosol models in the literature (Deshler et al., 1993; Wandinger et al., 1995; Omar et al., 2005; Sayer et al., 2012), were integrated. Since its inception, LIVAS has supported numerous studies related to dust climatology and retrieval optimization (Marinou et al., 2017; Proestakis et al., 2018; Moustaka et al., 2023; 2024), new dataset development (Fountoulakis et al., 2021; 2022; Papachristopoulou et al., 2022), and the evaluation of aerosol effects on solar radiation models (Konsta et al., 2018; Moustaka et al., 2024). In addition to the aerosol products, the temperature and pressure profiles (included in CALIOP auxiliary datasets) originating from the NASA Global Modeling and Assimilation Office (GMAO) meteorological analyses (NASA Langley Research Center, 2007) were also employed for the estimation of the molecular backscatter profiles required in Eq. (9), as discussed in detail in Section 3.3.

2.2 ModIs Dust AeroSol (MIDAS) dataset

The ModIs Dust AeroSol (MIDAS) dataset (Gkikas et al., 2021) was developed to focus specifically on dust aerosols by estimating dust optical depth (DOD) at a global scale and fine spatial resolution ($0.1^\circ \times 0.1^\circ$). The MIDAS product spans a 15-year period (2003–2017) and integrates MODIS-Aqua AOD retrievals with the dust-specific information from the Modern-Era Retrospective analysis for Research and Applications version 2 (MERRA-2) reanalysis, which provides the dust fraction

to the total aerosol load. The MIDAS development process includes multiple steps to ensure high-quality dust aerosol data, such as quality filtering, spatial and temporal colocation, and error estimation.

To generate the MIDAS DOD product, a synergy between MODIS-Aqua L2 AOD retrievals and MERRA-2 dust-to-total AOD ratios are employed. The integration of MODIS AOD with MERRA-2 dust fraction requires careful spatial and temporal colocation. Since MERRA-2 outputs are available at a coarser spatial resolution ($0.5^\circ \times 0.625^\circ$) compared to MODIS's fine-resolution grid ($10 \text{ km} \times 10 \text{ km}$), the nearest MERRA-2 grid points to the MODIS swath-level retrievals are selected. The time colocation also considers the nearest hourly MERRA-2 data corresponding to the MODIS overpass. The MIDAS product employs a series of filtering criteria to enhance the accuracy of its AOD retrievals from MODIS. First, only high-quality MODIS AOD data are used, based on quality assurance (QA) flags, where only retrievals with QA flags of "good" or "very good" are included. In addition, data points with cloud fractions greater than 0.8 or lacking adjacent retrievals are discarded to minimize cloud contamination, following the recommendations of earlier studies (Anderson et al., 2005; Zhang and Reid, 2006; Hyer et al., 2011; Shi et al., 2011).

MIDAS has been validated against ground-based AERONET data, showing a strong correlation ($R = 0.89$) and only a slight positive bias of 2.7% on a global scale (Gkikas et al., 2021). This demonstrates that the MIDAS product accurately represents dust aerosols, especially over key dust regions like North Africa, the Middle East, and Asia. The MIDAS dataset also offers an improvement over existing datasets by providing finer spatial resolution and more accurate dust-specific retrievals, while from its establishment it has supported a lot of studies focusing on dust climatology (Gkikas et al., 2022) and trends (Logothetis et al., 2021), model simulations in respect to emission and transport of dust particles (Kiriakidis et al., 2023) and dust impact on solar energy production (Masoom et al., 2021; Papachristopoulou et al., 2022). We exploit the MIDAS columnar DOD product at 550 nm, while CALIPSO provides observations at 532 nm. Given that pure dust is characterized by Ångström exponent values close to zero, the difference between 550 nm and 532 nm is expected to be negligible. For this study, we analyse the 550 nm DOD at a $1^\circ \times 1^\circ$ spatial resolution over the 10-year period (2007–2017), ensuring consistency with the CALIPSO mission, as MODIS-Aqua lowered its orbit relative to CALIPSO in early 2018, affecting their observational overlap.

190 **2.3 POLDER-3 and GRASP/Components**

The POLDER-3 (Polarization and Directionality of Earth's Reflectances) sensor, onboard the PARASOL (Polarisation and Anisotropy of Reflectances for Atmospheric Science coupled with Observations from a Lidar) satellite, was developed to improve the characterization of aerosol optical properties through multi-angle, multi-spectral, and polarimetric observations (Steinmetz et al., 2005; Chen et al., 2020; Dubovik et al., 2021; Zhang et al., 2021). POLDER-3 collected radiance measurements across six spectral channels (443, 490, 565, 670, 865 and 1020 nm) and polarization measurements at three channels (490, 670, and 865 nm), allowing it to provide unique insights into aerosol properties by capturing data from up to 16 viewing angles per pixel (Dubovik et al., 2011). This multi-angle capability facilitated global coverage every two days, offering valuable information about the size, shape, and composition of aerosol particles (Dubovik et al., 2011).

The Generalized Retrieval of Aerosol and Surface Properties (GRASP) algorithm, applied to POLDER-3 data, derives detailed
 200 aerosol and surface properties, with a component-based approach enhancing the characterization of aerosol properties
 (Dubovik et al., 2011). In this framework, aerosols are modeled as mixtures of various components—such as hydrated soluble,
 black carbon, brown carbon, and iron oxides—representative of different aerosol species and characterized by specific
 chemical compositions and known refractive indices (Dubovik et al., 2006; Schuster et al., 2016). The GRASP/Component
 algorithm provides daily retrievals of aerosol optical properties like aerosol optical depth (AOD), Ångström exponent (AE),
 205 fine-mode AOD (AODF), coarse-mode AOD (AODC), single scattering albedo (SSA) and refractive indices as well as detailed
 information on aerosol composition and particle size distribution in $0.1^\circ \times 0.1^\circ$ or $1^\circ \times 1^\circ$ spatial resolution from 2005 to 2013
 (Li et al., 2019; Dubovik et al., 2021).

In terms of validation, the GRASP/Component method has demonstrated strong agreement with AERONET stations,
 particularly for AOD, with negligible bias over both land and ocean (Li et al., 2019; Zhang et al., 2021). Fine-mode and coarse-
 210 mode AOD retrievals similarly align well with AERONET, and SSA and AE retrievals from GRASP exhibit high accuracy,
 enhancing the reliability of aerosol property assessments on a global scale (Li et al., 2019; Dubovik et al., 2021; Zhang et al.,
 2021). By utilizing advanced radiative transfer calculations without reliance on look-up tables, the GRASP/Component method
 has achieved high accuracy in aerosol property retrievals (Dubovik et al., 2021). In the present study, we exploit the L3 daily
 POLDER-3/GRASP-Component AOD retrievals at a $1^\circ \times 1^\circ$ spatial resolution for the period when the CALIPSO and
 215 PARASOL satellites were flying in tandem in the A-Train constellation (June 2006 – early December 2009). Since POLDER-
 3/GRASP-Component AOD is not provided exactly at 532 nm, the Ångström formula (Ångström, 1929) is applied on the
 available POLDER-3/GRASP wavelengths (i.e., 440, 670) to derive AOD at 532 nm for consistency with CALIPSO
 observations. Specifically, the interpolation of AOD at 532 is articulated through the following equations:

$$\mathring{a} = -\frac{\ln\left(\frac{AOD_{\lambda_0}}{AOD_{\lambda_1}}\right)}{\ln\left(\frac{\lambda_0}{\lambda_1}\right)}, \quad (1)$$

$$AOD_\lambda = AOD_{\lambda_0} \cdot \left(\frac{\lambda_0}{\lambda}\right)^{\mathring{a}}, \quad (2)$$

where λ refers to the 532 nm, λ_0 to the 440 nm, λ_1 to the 670 nm and \mathring{a} is the Ångström exponent across the 440-670 nm
 220 wavelength range.

3 Methodology

Our region of interest (ROI) encompasses the major and most active deserts of the planet situated in North Africa and in the
 broader region of the Middle East (Ginoux et al., 2012), as illustrated in Fig. 1. ROI hosts major dust sources, primarily over
 North Africa (yellow-shaded area), including the Bodélé Depression in the northern Chad Basin, the eastern Libyan Desert,
 225 the Nubian Desert, and parts of western Africa. In the Middle East (purple-shaded area), significant sources include the Arabian

Desert, with the Rub' al Khali and the Mesopotamian region between the Tigris and Euphrates rivers, as well as the deserts of western Central Asia, notably the Karakum and Kyzylkum (Ginoux et al., 2012; Hamidi et al., 2013; Gkikas et al., 2022). Subsequently, based on the CALIPSO aerosol subtype product, we focus on dust cases, and finally we adjust the dust LR such as the CALIOP DOD at 532 nm to match the columnar DODs from MIDAS and POLDER-3/GRASP. Dust is the most well-
230 characterized subtype of the CALIPSO aerosol product (Burton et al., 2013), due to the accurate depolarization measurements of CALIOP, which enable the detection of non-spherical dust layers. The AOD products from MIDAS and POLDER-3/GRASP have also demonstrated a strong performance in assessment studies against AERONET observations (Dubovik et al., 2011; Li et al., 2019; Gkikas et al., 2021; Zhang et al., 2021). A synergistic use of these active and passive sensors of the A-Train constellation can lead to the derivation of noteworthy dust LR patterns at 532 nm over the most well-known dust
235 regions around the globe.

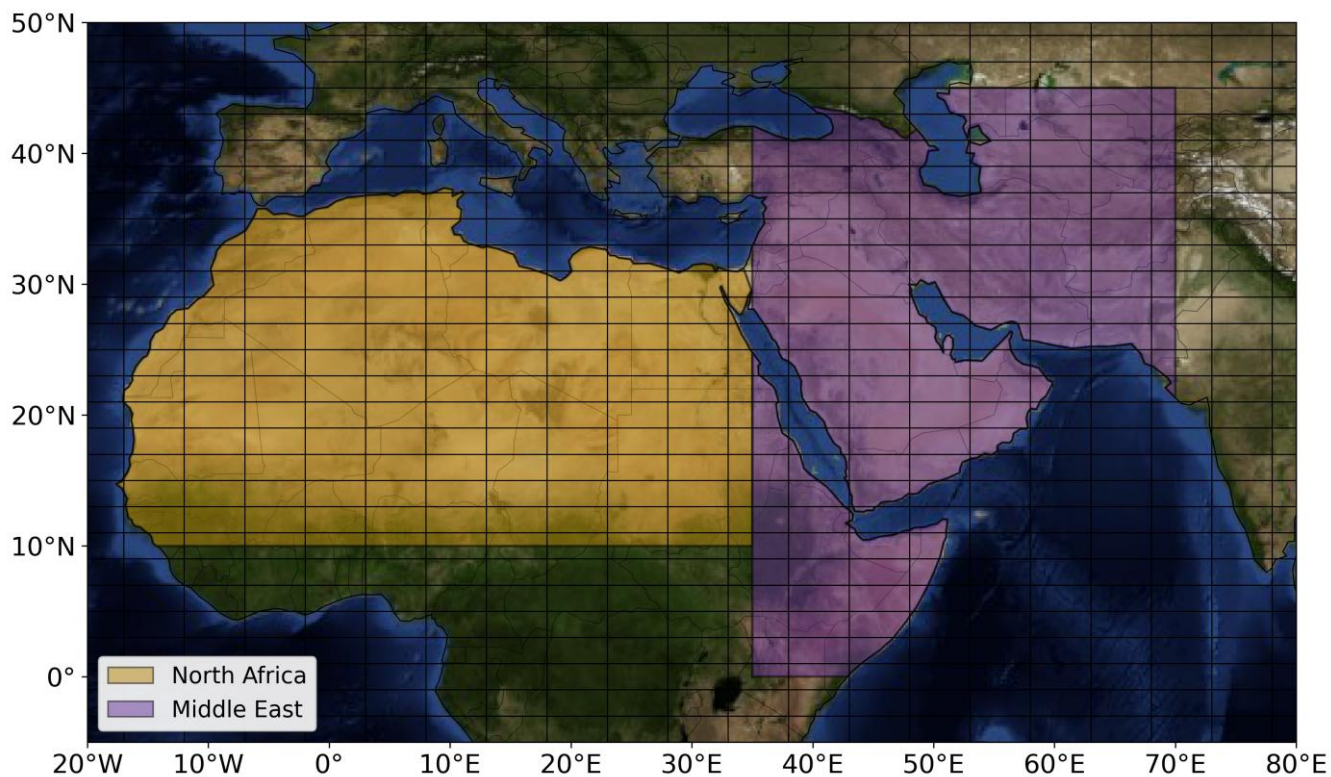


Figure 1: The North Africa (yellow-shaded area) and the Middle East (purple-shaded area) desert regions as defined based on Ginoux et al. (2012). The domain is divided into grids with $2^\circ \times 5^\circ$ spatial resolution grids based on Winker et al. (2013) in order to minimize the signal error in CALIPSO mean profiles. Map source: NASA Earth Observatory.

240 3.1 Definition of dust cases

Initially, the domain is divided into grids with $2^\circ \times 5^\circ$ spatial resolution, following the CALIPSO Level 3 (L3) official spatial resolution applied towards reducing the signal noise contamination in the mean vertical profiles (Winker et al., 2013; Tackett

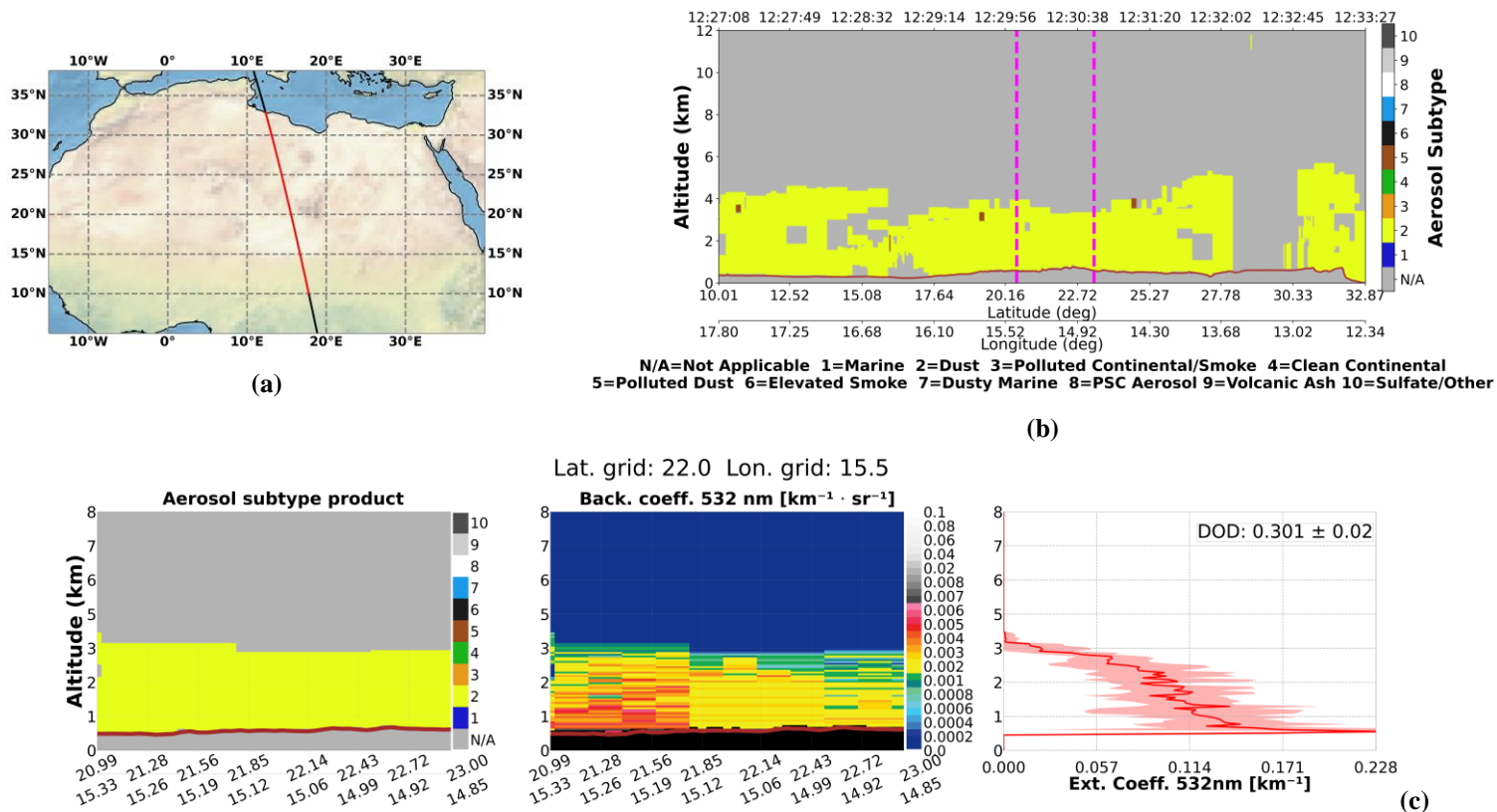
et al. 2018). The segments of the CALIPSO orbit traversing desert regions were identified. The corresponding Level-2 (L2) 5-km aerosol profiles were then grouped into predefined $2^\circ \times 5^\circ$ grids based on their geospatial coordinates. Considering the
245 segment of the orbit residing within each grid cell, the following criteria must be fulfilled for an overpass to be classified as a dust case:

- (i) dust classified atmospheric layers (based only on the aerosol subtype classification product of CALIPSO; Kim et al., 2018) should be at least the 95% of the total aerosol records,
- (ii) there should be no disturbance in mean profiles due to filtering processes (i.e., extinction profiles without any missing
250 vertical layer due to filtering along the overpass),
- (iii) there should be no clouds detected (“clear-sky” conditions), and
- (iv) CALIOP beam should be penetrating throughout the atmosphere reaching the Earth’s surface level.

In Fig. 2, we present, as an indicative example, one of the defined dust cases to illustrate the applied CALIOP-based processing for a specific grid cell over the Saharan Desert (center of the grid: lat 22.00, lon 15.5). For the part of the CALIPSO L2 5 km
255 aerosol profiles residing within the grid area (confined between the magenta vertical dashed lines in Fig. 2b), the CALIOP-provided extinction coefficient profiles at 532 nm are spatially averaged to derive a mean extinction coefficient vertical profile (Fig. 2c). Due to the strict filtering criteria applied for the definition of dust cases, we assume the sole presence of dust in the selected cases. Accordingly, the mean extinction coefficient profile is computed exclusively from atmospheric layers classified as “dust” by the CALIOP aerosol subtype algorithm (Kim et al., 2018), while contributions from dust mixtures (i.e., polluted
260 dust and dusty marine) are excluded. This approach, supported by consistently high particulate depolarization ratios (> 0.27 ; Fig. S1) observed in the selected cases, ensures that the retrieved extinction profiles are representative of pure dust aerosols. Within this framework, the mean extinction coefficient profile retrieved for the identified dust cases is hereafter referred to as dust extinction throughout the remainder of the study.

The dust extinction coefficient profiles (α_{CALIOP}^d) and their associated uncertainties ($\sigma_{\alpha, CALIOP}^d$) used in this study are provided
265 within the LIVAS dataset. Once the mean dust extinction coefficient profile is obtained for the selected dust layers within the grid, it is vertically integrated to derive the corresponding DOD at 532 nm for each identified dust case. It should be noted that the vertical integration is performed only over the atmospheric layers identified as containing dust — potentially spanning multiple non-contiguous layers — while dust-free regions in between, above, or below the dust layers do not contribute to the DOD.

CALIPSO orbit: 2008-04-17T12-02-27ZD



270 Figure 2: (a) A single CALIPSO orbit (2008-04-17T12-02-27ZD) over North Africa (the part of the orbit falling inside the desert
 275 region is colored red), (b) the respective aerosol subtype curtain plot for the red part of the orbit, and (c) the part of the orbit falling
 inside a specific grid (center of the grid → lat: 22.00, lon: 15.5), defined with the two magenta vertical dashed lines in (b). The CALIPSO
 V4 aerosol subtype product (left panel) indicating the presence of pure dust (N/A: not an aerosol layer, 1: marine, 2: dust, 3: polluted
 continental/smoke, 4: clean continental, 5: polluted dust, 6: elevated smoke, 7: dusty marine, 8: PSC aerosol, 9: volcanic ash, 10:
 sulfate/other) and the backscatter coefficient 532 nm [$\text{km}^{-1} \cdot \text{sr}^{-1}$] (central panel). Vertical profile of the spatially averaged extinction
 coefficient 532 nm (right panel) along with its standard deviation (red-shaded area) for the respective orbit, along with the
 corresponding columnar DOD based on CALIPSO dust LR (44 sr).

3.2 Match-Up Methodology and DOD Uncertainty Estimation

280 After the identification of the dust cases based on CALIPSO, we identify the coincident $1^\circ \times 1^\circ$ products from MIDAS (DOD)
 and POLDER-3/GRASP (AOD) datasets. For MIDAS, we check the 10-year period spanning from 2007 to 2017, while for
 the POLDER-3/GRASP, the collocated period starts in June 2006 and ends in December 2009, as this marks the point when
 the PARASOL satellite's orbit was lowered to under the A-Train constellation. Additional to MIDAS and CALIPSO DOD, as
 long as we focus on the solely presence of dust particles based on CALIOP aerosol subtype algorithm, and we search for
 coincident POLDER-3/GRASP products, we can refer to DOD instead of the term of AOD for its retrievals.

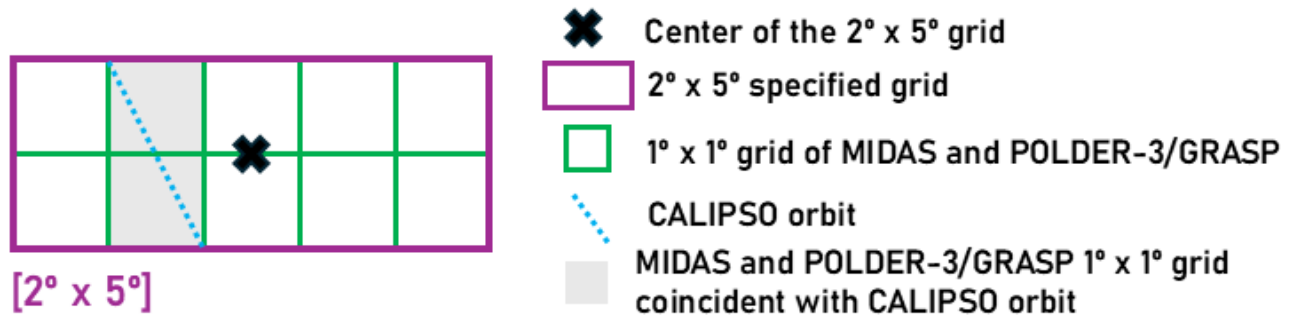
285 The match-up procedure is thoroughly presented in Fig. 3, while the filters that are applied on the $1^\circ \times 1^\circ$ MIDAS and POLDER-3/GRASP grids for quality assurance control and for the extraction of coastal pixels are outlined in Table 1. A random $2^\circ \times 5^\circ$ predefined grid is presented (purple square), divided into 10 subgrids with $1^\circ \times 1^\circ$ spatial resolution (green squares), which is the resolution of MIDAS and POLDER-3/GRASP products utilized in the current study. For a specific CALIPSO orbit (cyan points), the grey shaded $1^\circ \times 1^\circ$ grids are those from passive sensors (MIDAS, POLDER-3/GRASP).

290 For these grids to be included in the mean columnar DOD computation from MIDAS and POLDER-3/GRASP products, they must meet the criteria outlined in Table 1. The “LandPercentage” and “Land_sea_Flag” filters are applied to POLDER-3/GRASP and MIDAS products respectively, to exclude coastal pixels. Additionally, a threshold of 0.05 for “ResidualRelative” (the mean root square of relative error from fitting POLDER-3 non-polarised radiance measurements by the GRASP algorithm) is applied as recommended in several studies (Dubovik et al., 2011; Chen et al., 2020; Zhang et al.,

295 2021) to ensure more reliable aerosol retrievals. For MIDAS product, no additional criteria need to be employed in the filtering process, as long as during its development only high-quality data were used (Gkikas et al., 2021). If there is at least a single $1^\circ \times 1^\circ$ grid fulfilling the aforementioned criteria, we process to the computation of the mean columnar DOD from MIDAS and POLDER-3/GRASP products and these values are assigned to the $2^\circ \times 5^\circ$ predefined grid.

300 **Table 1: Filters applied on POLDER-3/GRASP and MIDAS products to select quality-assured data while ensuring the elimination of coastal regions.**

POLDER-3/GRASP	“ResidualRelative” < 0.05 “LandPercentage” = 100
MIDAS	“Land_sea_Flag” = 1



305 **Figure 3: Schematic representation of the spatial match-up methodology used to compare CALIPSO-derived aerosol properties, provided on a predefined $2^\circ \times 5^\circ$ grid (outlined in purple), with the higher-resolution $1^\circ \times 1^\circ$ grids of the MIDAS and POLDER-3/GRASP products (outlined in green). The black cross marks the center of the selected CALIPSO $2^\circ \times 5^\circ$ grid cell. The blue dashed line represents the CALIPSO satellite orbit. MIDAS and POLDER-3/GRASP $1^\circ \times 1^\circ$ grid cells that intersect the CALIPSO orbit are highlighted in light grey. Only the coincident $1^\circ \times 1^\circ$ grid cells within the selected $2^\circ \times 5^\circ$ region are considered for the match-up.**

Following the match-up methodology between the A-Train satellite constellation, the methodology used to estimate the

310 absolute (σ_i^{DOD}) and relative uncertainties (σ_i^{rel}) of the DOD products employed in this study —with i denoting either CALIOP, POLDER-3/GRASP, or MIDAS—for each collocated dust case is presented. These uncertainties are used as a

quantitative criterion to retain only “reliable” retrievals in the subsequent comparisons, as well as a direct input to the Monte Carlo framework employed for the estimation of the random uncertainty of LR retrieval, as described in Section 3.3.2. A consistent uncertainty characterization is therefore essential for both the quality control of the datasets and the robustness of the LR uncertainty assessment.

For CALIOP, the absolute uncertainty of DOD (σ_{CALIOP}^{DOD}) is estimated by propagating the extinction uncertainties provided by the LIVAS dataset through the numerical vertical integration scheme. Assuming uncorrelated errors between the vertical levels, the propagated absolute uncertainty is given by:

$$\sigma_{CALIOP}^{DOD} = \Delta z \cdot \sqrt{\sum_{i=1}^N \sigma_{\alpha_i}^2 - \frac{\sigma_{\alpha_1}^2 + \sigma_{\alpha_N}^2}{2}}, \quad (3)$$

where σ_{α_i} denotes the uncertainty of the dust extinction coefficient at altitudinal level i , Δz is the vertical resolution of the CALIOP profile, and N is the total number of vertical levels contributing to the integration. The DOD relative uncertainty (σ_{CALIOP}^{rel}) is then defined as:

$$\sigma_{CALIOP}^{rel} = \frac{\sigma_{CALIOP}^{DOD}}{\sqrt{N} \cdot DOD_{CALIOP}}, \quad (4)$$

where N is the number of CALIOP profiles overpassing each $2^\circ \times 5^\circ$ predefined grid.

For MIDAS, the DOD uncertainties ($\sigma_{MIDAS}^{DOD}; \sigma_{MIDAS}^{rel}$) are estimated following the uncertainty parameterizations adopted for the MODIS Dark Target (DT) and Deep Blue (DB) aerosol products, assuming constant coefficients representative of barren soils and a fixed geometric airmass factor (AMF) equal to 2.8 (Sayer et al., 2013). The absolute uncertainty of the DT component is expressed as:

$$\sigma_{DT} = 0.15 \cdot DOD_{MIDAS} + 0.05, \quad (5)$$

while the corresponding DB uncertainty is given by:

$$\sigma_{DB} = \frac{a + b \cdot DOD_{MIDAS}}{AMF}, \quad (6)$$

where a and b are empirical coefficients that depend on the surface type and AMF is the geometric airmass factor. In this study, since our analysis is performed over the major deserts of the planet (see Fig. 1), constant values representative of barren soils are adopted for a and b , equal to 0.12 and 0.61, respectively, following Gkikas et al. (2021).

For the merged MIDAS product, the total absolute uncertainty (σ_{MIDAS}^{DOD}) is obtained from the quadrature sum of the DT and DB components:

$$\sigma_{MIDAS}^{DOD} = \frac{1}{2} \sqrt{\sigma_{DT}^2 + \sigma_{DB}^2}. \quad (7)$$

Finally, the relative MIDAS DOD uncertainty (σ_{MIDAS}^{rel}) is computed as:

$$\sigma_{MIDAS}^{rel} = \frac{\sigma_{MIDAS}^{DOD}}{\sqrt{N} \cdot DOD_{MIDAS}}, \quad (8)$$

where N is the number of $1^\circ \times 1^\circ$ MIDAS grids within each $2^\circ \times 5^\circ$ predefined grid, fulfilling the criteria discussed at the beginning of this section.

For POLDER-3/GRASP, the DOD uncertainties ($\sigma_{POLDER-3/GRASP}^{DOD}; \sigma_{POLDER-3/GRASP}^{rel}$) are estimated following the same general framework adopted for MIDAS (Gkikas et al., 2021). Different empirical coefficients are employed, following Zhang et al. (2021), with $a = 0.008$ and $b = 0.892$, to account for the specific characteristics of the POLDER-3/GRASP product. In addition, a constant AMF equal to 2.92 is adopted, based on an independent analysis of POLDER viewing geometries derived from a one-year dataset over 19 AERONET stations (Fig. S2).

As an example, the relative DOD uncertainties for the CALIOP–MIDAS synergy are presented in Fig. 4. The red dashed vertical line indicates the relative uncertainty threshold value of 0.5 used for the selection of reliable DOD retrievals. This threshold was selected to retain a statistically significant number of cases for the derivation of the dust LR_s using the methodology presented in the following section. Additionally, the relative uncertainties for the CALIOP-POLDER-3/GRASP synergy are presented in Fig. S3.

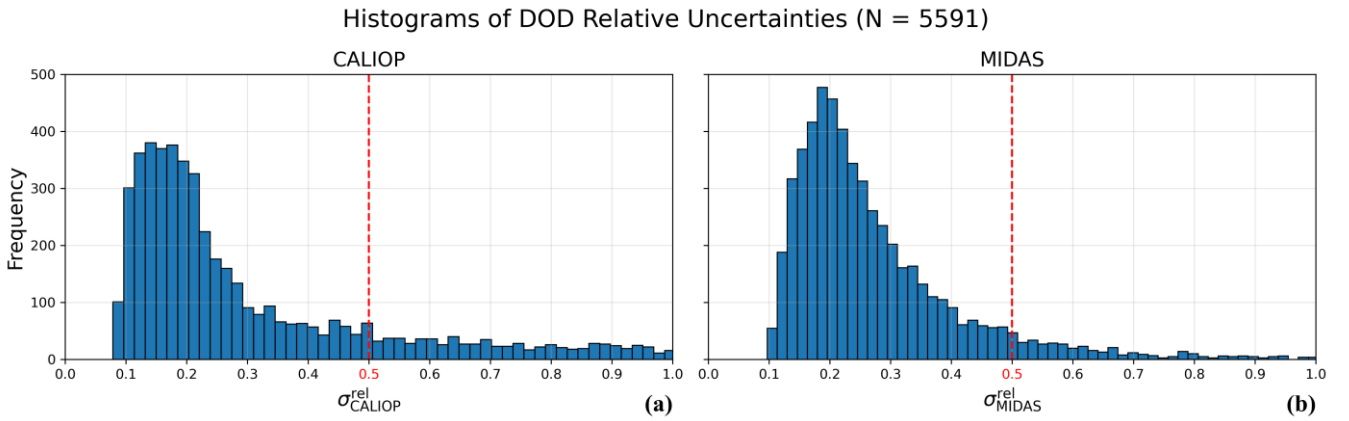


Figure 4: Histograms of the relative dust optical depth (DOD) uncertainties for (a) CALIOP (σ_{CALIOP}^{rel}) and (b) MIDAS (σ_{MIDAS}^{rel}) for the total 5,591 dust cases identified over North Africa and the Middle East. The red vertical dashed line indicates the relative uncertainty threshold value of 0.5 used for the selection of reliable DOD retrievals.

3.3 Dust lidar ratio retrieval method

The calculation of dust LR is based on minimizing the Y function of Eq. (S2.14) of the Supplement, also introduced here as Eq. (9). We note that the parameters in Eq. (9) differ from those in the Supplement because in our study the formulation is specialized to dust-only cases and to the CALIOP-MIDAS and CALIOP-POLDER-3/GRASP synergies. The general formulation presented in the Supplement, however, remains applicable to other aerosol species and datasets. The Eq. (9) is modified as follows:

$$Y = \left| DOD_{CALIOP} - LR_{CALIOP}^d \int_{z_o}^{z_G} \left\{ \frac{\left(\frac{\alpha_d}{LR_{eff}^d} + \beta_m \right) \exp \left[-2 \int_{z_o}^z (\alpha_d + LR_{CALIOP}^d \beta_m) d\zeta \right]}{1 - 2LR_{CALIOP}^d \int_{z_o}^z \left(\frac{\alpha_d}{LR_{eff}^d} + \beta_m \right) \exp \left[-2 \int_{z_o}^{\zeta} (\alpha_d + LR_{CALIOP}^d) d\zeta' \right] d\zeta} - \beta_m \right\} dz \right| \quad (9)$$

Here, the parameter z is the range from the spaceborne lidar, ζ and ζ' are both surrogate variables representing different instances of range in the nested integrals, z_o is the reference (aerosol free) range corresponding to the highest altitude of the CALIOP profile (≈ 30 km), z_G is the ground range, β_m is the vertically resolved molecular backscatter coefficient, α_d is the particle extinction coefficient, LR_{CALIOP}^d is the constant dust LR (i.e., 44 sr - Kim et al., 2018), LR_{eff}^d is the effective columnar dust LR, and DOD_{CALIOP} is the CALIOP DOD. The z reference system is discussed in the Supplement.

To minimize the function Y we try different LR_{eff}^d values and select the one that results to the Y value closest to zero. As discussed in Section 2.1, the pressure and temperature profiles within CALIPSO dataset are used for the calculation of β_m . The dust extinction coefficient (α_d) is not available from MIDAS or POLDER-3/GRASP; however, the CALIOP extinction profile (α_{CALIOP}^d) can be scaled using the reference DOD_i (where i denotes either MIDAS or POLDER-3/GRASP) and used as a priori extinction information. The errors introduced by this assumption are discussed in Section 3.3.1. The following physical constraints have been applied for the inversion:

- (i) The values of LR_{eff}^d are restricted to the range of 20–68 sr. This range represents ± 24 sr around the constant dust LR of 44 sr used within CALIPSO algorithm (Kim et al., 2018). Moreover, this range encompasses dust LRs reported in previous studies, including 53.1 ± 7.9 sr for Saharan dust and 37.4 ± 5.3 sr for Middle Eastern dust, as summarized in Floutsis et al. (2023),
 - (ii) the LR_{eff}^d values which cause the denominator of Eq. (9) to become lower than 0.01 are automatically rejected. Such LR_{eff}^d values would lead to parts of the α_{CALIOP}^d and β_{CALIOP}^d profiles approaching infinity or becoming negative, which were never observed in our CALIPSO dataset, and
 - (iii) the Y minimum must be smaller than 0.01 to guarantee that it is sufficiently close to zero.
- The second and third constraint become more important when random uncertainty of the retrieval is considered (see Section 3.3.2).

3.3.1 Systematic uncertainty of the lidar ratio retrieval

The systematic uncertainty introduced from the retrieval of LR_{eff}^d has been evaluated using synthetic β_d and α_d profiles whose dust lidar ratio LR_d was assumed to be constant with height. The LR_d and DOD_i were assumed to range between 20 and 68 sr and between 0.1 and 1, respectively. We did not consider testing the function outside the 20–68 sr range, as such values deviate substantially from the reference LR_{CALIOP}^d of 44 sr commonly used in the Klett retrieval (Kim et al., 2018) and from dust LR values reported in the literature (Floutsis et al., 2023). We also did not consider DOD values higher than 1 because they rarely appear in our datasets. For the simulation of the molecular backscatter β_m , pressure and temperature profiles generated by the

U.S. Standard Atmosphere (1976) were applied. Those α_d and β_m profiles were used to simulate the range-corrected lidar signal that a satellite lidar would measure and to simulate the corresponding β_{CALIOP}^d and DOD_{CALIOP} when the forward Klett inversion is applied. Then, considering α_d and β_m to be known, Eq. (9) was used to retrieve the effective columnar dust lidar ratio LR_{eff}^d . The systematic bias is calculated from the difference between LR_d and LR_{eff}^d . It was found that if α_d and β_m are accurately known, the retrieval uncertainty of LR_{eff}^d is also very accurate, with a systematic bias less than 0.1 sr. This check was done to ensure the overall validity of Eq (9).

Our application, however, is not so simple as only the biased Klett extinction coefficient profile α_{CALIOP}^d is available in the CALIPSO dataset. We have examined how accurately can LR_{eff}^d be retrieved when applying α_{CALIOP}^d scaled with DOD_i instead of α_d as a priori extinction profile to function Y . We have seen that this is a much better approximation than using no a priori information on the aerosol vertical distribution at all, leading to a systematic bias less than 1 sr for any LR_d within 20–68 sr and for any DOD_i within 0.1 and 1, which is sufficient for the purposes of this study.

3.3.2 Random uncertainty of the lidar ratio retrieval

The random uncertainty is calculated with a Monte Carlo approach. The input data used for the calculation of LR_{eff}^d include: the α_{CALIOP}^d , DOD_i (from either MIDAS or POLDER-3/GRASP), and the pressure and temperature profiles provided in the CALIPSO dataset (as discussed in Section 2.1). The absolute uncertainty of α_{CALIOP}^d ($\sigma_{\alpha_{CALIOP}^d}^d$) for each dust case is provided within the LIVAS dataset, while the uncertainty of DOD_{CALIOP} is estimated through Eq. (3); both representing absolute random uncertainties. To assess the random uncertainty $\sigma_{LR}^{d,eff}$ of LR_{eff}^d we perform 100 Monte Carlo permutations (indicated by index j) assuming that the error distributions of α_{CALIOP}^d and DOD_i are Gaussian and that $\sigma_{\alpha_{CALIOP}^d}^d$ and σ_i^{DOD} correspond to one standard deviation. The $LR_{eff,j}^d$ that minimizes Y_j is calculated for each permutation j . Then, $\sigma_{LR}^{d,eff}$ is estimated as the standard deviation of the LR_{eff} error distribution. The physical constraints mentioned early in section 3.3 become important when estimating the random uncertainty because they ensure that no $LR_{eff,j}^d$ without physical meaning participate in the error distribution.

3.3.3 Propagation of grid-cell-level uncertainties

To quantify the uncertainty of the spatiotemporally averaged dust LR, we propagate the grid-cell-level uncertainties through the temporal and spatial averaging steps. Each grid cell may be sampled multiple times by different number of dust cases (selected based on the criteria discussed in Section 3.1), and the uncertainty of the mean dust LR therefore depends both on the uncertainties of the individual cases and on the sampling variability within the grid cell.

Following Gkikas et al. (2022), the uncertainty of the temporally averaged dust LR in grid cell i is computed as:

$$\sigma'_i = \frac{\sqrt{\sum_{k=1}^{N_i} (\sigma_{LR,i,k}^{d,eff})^2}}{N_i}, \quad (10)$$

where N_i is the number of dust cases in grid cell i , and $\sigma_{LR,i,k}^{d,eff}$ denotes the uncertainty of the effective dust LR for case k within the i -th grid-cell.

In addition, we account for sampling uncertainty using the standard error of the mean (SE):

$$SE_i = \frac{SD_i}{\sqrt{N_i}}, \quad (11)$$

415 where SD_i is the standard deviation of the dust LR values from all the dust cases within grid cell i .

The total uncertainty (σ) of grid cell i is then given by:

$$\sigma_i = \sqrt{(\sigma'_i)^2 + (SE_i)^2}. \quad (12)$$

Finally, when computing spatial averages at regional scales, we assume that the grid-cell uncertainties are correlated across space. Under this assumption, the uncertainty of a spatially averaged dust LR is obtained by taking the area-weighted mean of the individual grid-cell uncertainties. For a spatial domain j containing N_j grid cells, the corresponding uncertainty is:

$$\sigma_j = \sum_{i=1}^{N_j} w_i \cdot \sigma_i, \quad (13)$$

420 where w_i represents the weight of grid cell i , defined as the fraction of dust cases in grid cell i relative to the total number of dust cases within the region.

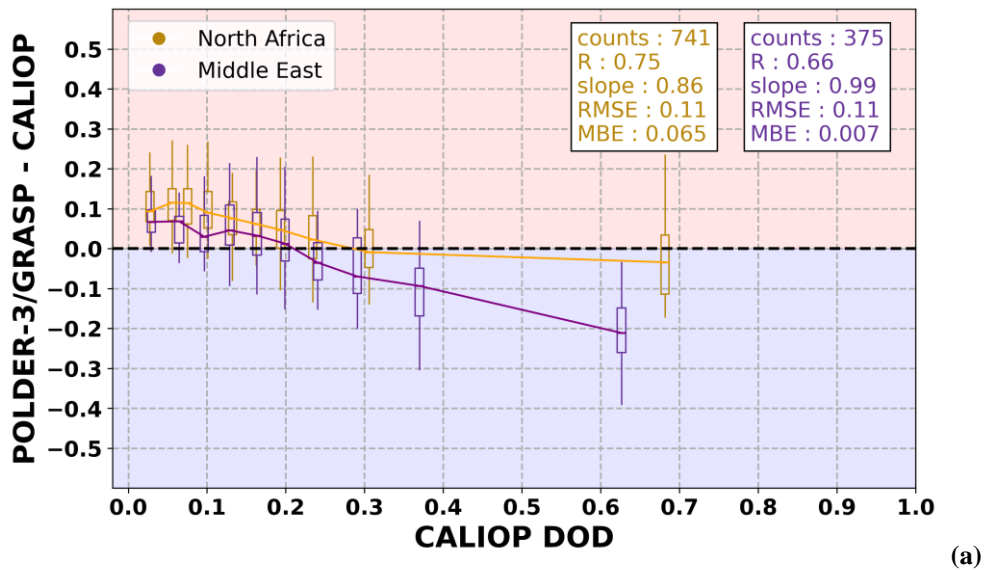
4 Results

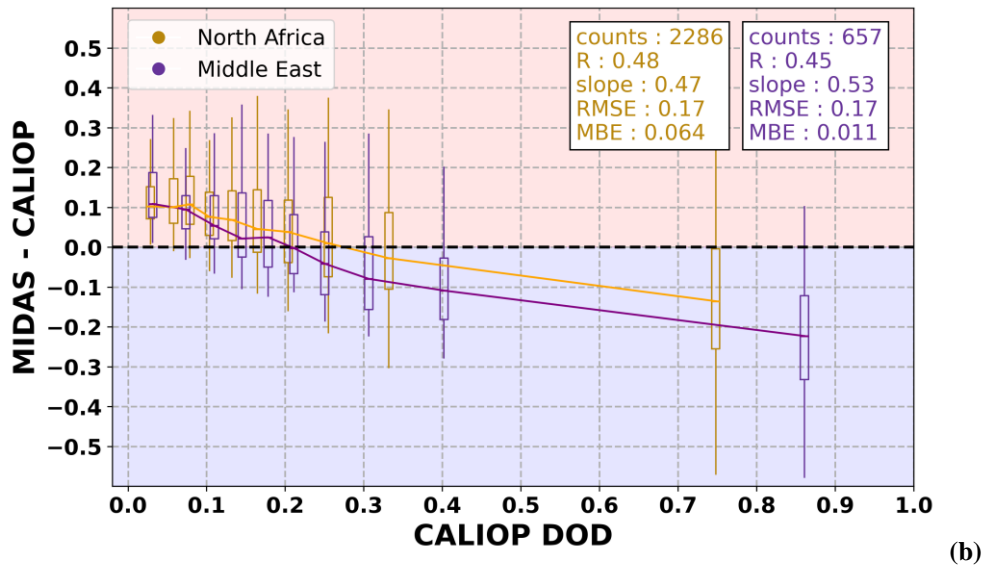
4.1 Examination of DOD retrievals among the A-Train constellation

The methodology described in Section 3 yielded a sample of 2,943 and 1,116 collocated pairs between CALIOP-MIDAS and
 425 CALIOP-POLDER-3/GRASP, respectively. In Figure 5, we present the box-whisker plots of the DOD_{diff} (defined as $DOD_i - DOD_{CALIOP}$, where i refers to either MIDAS or POLDER-3/GRASP) (y axis) between the two synergies of CALIOP-POLDER-3/GRASP (Fig. 5a) and CALIOP-MIDAS (Fig. 5b) divided into 10 equal-sized bins by CALIOP DODs (x axis). The obtained statistics are provided separately for North Africa (yellow color) and Middle East (purple color), including the slope of the linear regression, the Mean Bias Error (MBE), the correlation coefficient (R) and the Root Mean Square Error
 430 (RMSE), along with the number of collocated samples per region (counts). Based on the statistics, there is a pronounced underestimation of CALIOP DODs over North Africa (MBE equal to +0.065 and +0.064 for CALIOP-POLDER-3/GRASP and CALIOP-MIDAS synergy, respectively) indicating that higher dust LRs over the region could improve the CALIOP DOD retrievals. Over the Middle East, CALIOP DODs are also underestimated by both synergies; however, the biases are significantly smaller in respect to North Africa (MBE equal to +0.007 and +0.011 for CALIOP-POLDER-3/GRASP and

435 CALIOP-MIDAS synergy, respectively). While the outcome over North Africa is in good agreement with previous studies based on ground-based lidar observations, a contrasting pattern is observed over the Middle East, with earlier studies reporting lower dust LR values (Müller et al., 2007; Groß et al., 2011; Preißler et al., 2011; Tesche et al., 2009, 2011; Kanitz et al., 2013; Baars et al., 2016; Rittmeister et al., 2017; Kaduk, 2017; Haarig et al., 2017a; Urbanneck, 2018; Bohlmann et al., 2018; Filioglou et al., 2020; Szczepanik et al., 2021; Haarig et al., 2022). Based on these studies, lower dust LRs (<44 sr) have generally been proposed over the Middle East, while higher values (> 44 sr) have been reported over North Africa. It should be noted, however, that these observations were mostly conducted far from major dust source regions and for individual dust cases originating from specific source areas. In contrast, our analysis spans a much broader spatial domain, encompassing most of North Africa and the Middle East, and therefore reflects regionally integrated dust conditions rather than isolated source-specific events.

445





450 **Figure 5:** Box-whisker plots for the dust optical depth differences (DOD_{diff}) (y-axis) (displaying the 75/25 percentiles at the boxes, and the median in the center line, while the whiskers are displaying the ± 1.5 IQR from the 25/75 percentiles, respectively) between (a) CALIOP – POLDER-3/GRASP and (b) CALIOP-MIDAS, along the CALIOP DODs (x-axis). The yellow boxes are assigned for North Africa, while the purple ones for Middle East. The background color denotes the over-/underestimation (red/blue color). The number of collocated measurements, the correlation coefficient (R), the slope of the linear regression, the Mean Bias Error (MBE), and the Root Mean Square Error (RMSE) scores are provided in the legends separately for North Africa and the Middle East.

4.2 Geographical distribution of the dust lidar ratio

455 Following Eq. (9), a mean dust LR value at 532 nm was computed for each $2^\circ \times 5^\circ$ grid over North Africa and Middle East domains (Fig. 1), along with its corresponding uncertainty metrics, and the number of the available dust cases. The LR geographical distribution of the differences between the upgraded dust LR (obtained via the CALIOP-POLDER-3/GRASP and CALIOP-MIDAS synergies, respectively) and the default value (44 sr) assigned to dust aerosols in the CALIPSO retrieval algorithm were also estimated. For the 10-year period of the CALIOP-MIDAS synergy, both annual and seasonal LR maps were produced. The corresponding dust LR maps and their uncertainties derived from the CALIOP-POLDER-3/GRASP synergy are also provided in the Supplement (Figs. S4–S5). However, due to the much shorter period of CALIPSO-PARASOL

460 satellites coincidence (2006–2009) and the substantially smaller number of available dust cases (1,116 instead of 2,943 for CALIOP–MIDAS), these maps are not analysed in detail here. Their use is limited to the regional LR assessment in Sect. 5, where the number of coincident retrievals within each predefined region remains relatively sufficient to derive meaningful statistics.

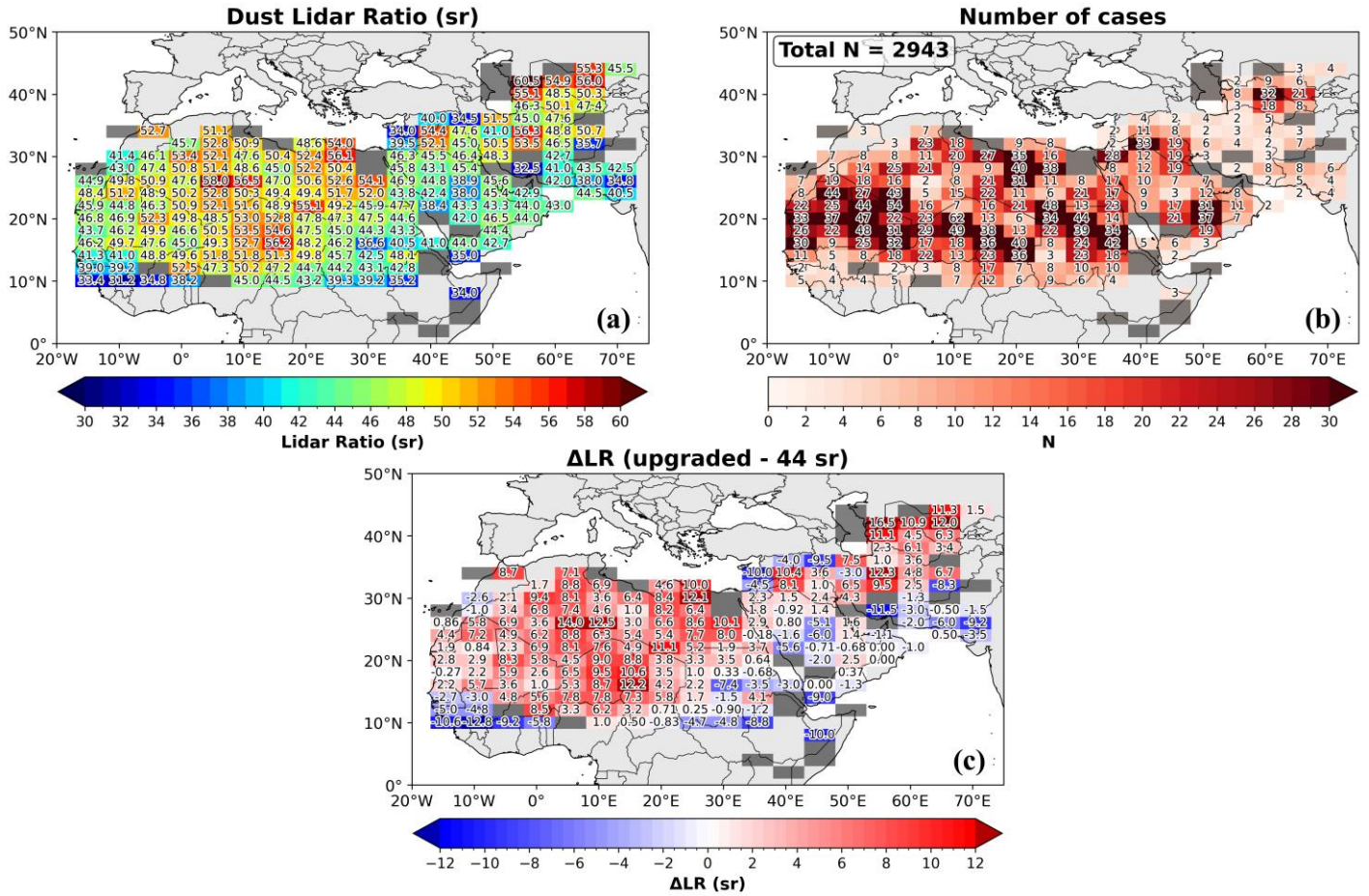
465 In Fig. 6a, the mean dust LR map from the CALIOP-MIDAS synergy is illustrated. Dust LRs are maximized (up to ~ 56 sr) over or near the strongest dust source globally (Washington et al., 2009; Ginoux et al., 2012), namely the Bodélé Depression in the northern Chad basin. Other North African desert regions yielding high dust LRs include the Grand Erg of Bilma and the basin of the Aïr (both over Niger), the Libyan desert, and regions in Sudan. On the western side of North Africa, notable areas

are the Erg El Djouf (over Mali and Mauritania) and the Grand Erg Occidental (over Algeria), all characterized by LR values mostly in the range of 47–52 sr. Even in the absence of ground-based dust LR measurements over the central Sahara and the major Saharan source regions (e.g., Bodélé), campaign-based studies, such as SAMUM-1/2 (Ansmann et al., 2011) and SALTRACE (Weinzierl et al., 2017), investigating the optical and microphysical properties of North African dust after short- and long-range transport reported LR values of 53.1 ± 7.9 sr, which fall well within the range of our CALIOP–MIDAS dust LR estimates. Across the Arabian Peninsula, the retrieved dust LR values exhibit pronounced spatial variability, with lower values (~38–45 sr) mainly in the central and southern parts, and locally higher values (~46–54 sr) toward the northern Arabian Peninsula and Mesopotamia. Overall, these values show regional agreement with ground-based lidar observations over the Arabian Peninsula, which reported dust LR values of 37.4 ± 5.3 sr (Müller et al., 2007; Kaduk, 2017; Urbanneck, 2018; Filioglou et al., 2020; Floutsi et al., 2023); however, not all retrieved dust LRs fall strictly within this literature-based range, particularly over the northern part of the region. Over the Central Asian deserts (Karakum and Kyzylkum), LR values typically range between ~47 and 56 sr. This region is considered relatively understudied in terms of dust LR, with the only available ground-based constraints provided by Hofer et al. (2020), who reported values in the range of ~35–40 sr over Dushanbe (Tajikistan) in the framework of the CADEX (Central Asian Dust Experiment) campaign (Althausen et al., 2019). Notably, one of our closest retrieved CALIOP–MIDAS dust LR values over this region is ~36 sr, which agrees remarkably well with these ground-based observations. At the same time, our analysis also reveals locally higher LR values across parts of Central Asia, which is consistent with the findings of Kim et al. (2020), who retrieved dust lidar ratios over the region using a synergistic CALIPSO–MODIS approach over a 5-year period.

The robustness of LR spatial patterns is supported by the number of collocated CALIOP–MIDAS dust cases per grid (Fig. 6b), which shows that most of North Africa and large parts of the Middle East are characterized by moderate to high sampling densities, frequently exceeding 20–40 cases per grid and locally reaching even higher values over the major dust sources of North Africa. This confirms that the derived dust LR values are not driven by isolated events but reflect climatologically persistent dust conditions (a conclusion further supported by the uncertainty analysis discussed below- see Fig. 7). In contrast, marginal sampling is mainly confined to peripheral regions, such as the Horn of Africa and parts of South and Central Asia, where the number of available dust cases is limited.

The spatial distribution of the LR deviations relative to the CALIOP default dust lidar ratio of 44 sr (Δ LR; Fig. 6c) provides direct insight into the regional adequacy of the fixed-LR assumption. Over most of North Africa, Δ LR is systematically positive, frequently exceeding +5 to +6 sr and locally over +10–12 sr over the Bodélé Depression and parts of the Libyan desert. This demonstrates that the default CALIOP dust LR of 44 sr systematically underestimates the effective dust LR over the major Saharan dust sources. This finding is fully consistent with the positive CALIOP DOD biases identified earlier (Fig. 5b) and supports the use of higher LR values over North Africa. In contrast, over large parts of the Arabian Desert, Δ LR is negative, with typical values ranging between -2 and -6 sr over the Arabian Peninsula and locally reaching -8 to -10 sr over parts of Iran and Afghanistan. Significant local reversals of this pattern are, however, observed over Mesopotamia and the Central Asian deserts, where positive Δ LR values reach up to approximately +16 sr.

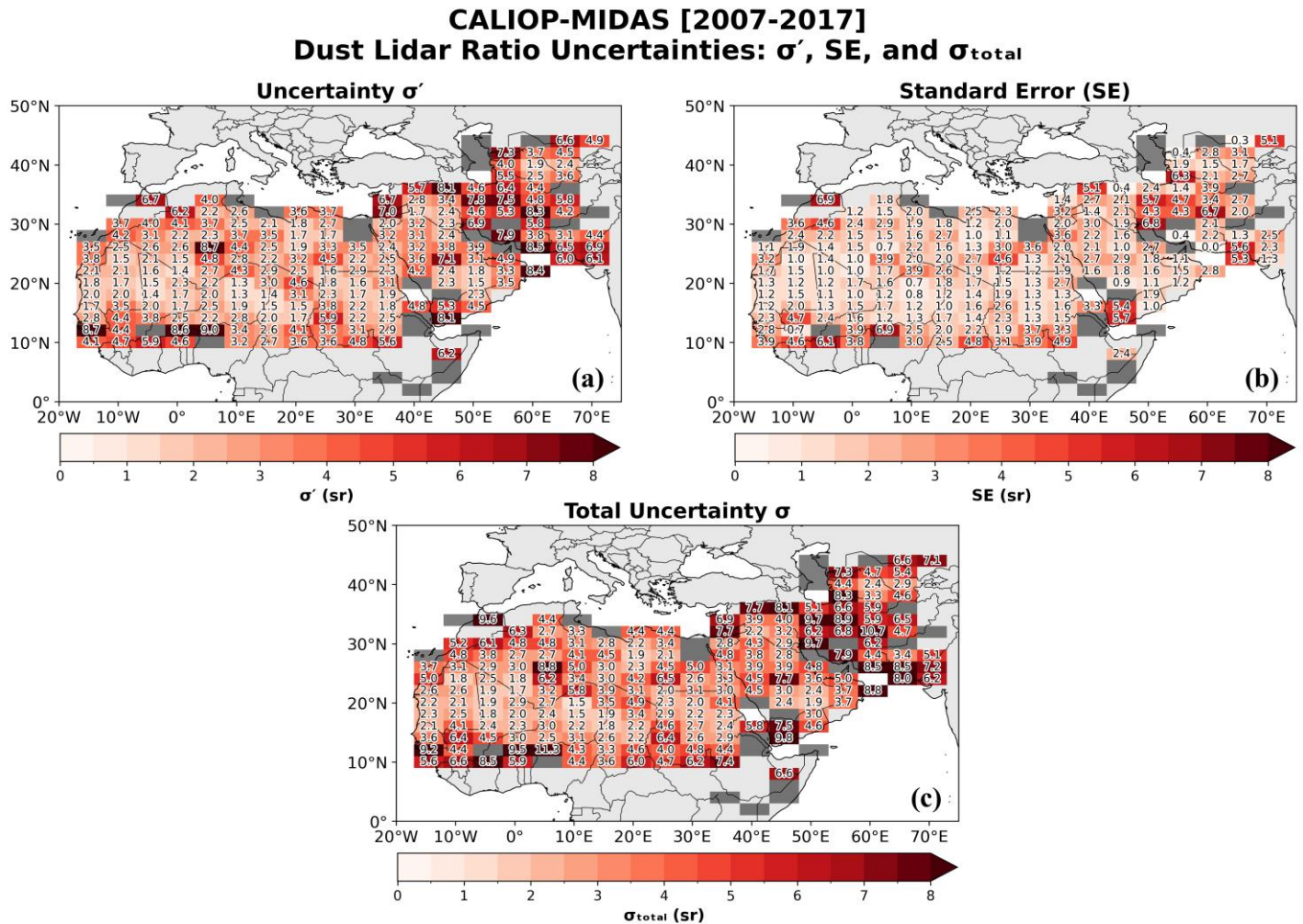
CALIOP-MIDAS [2007-2017]
Dust Lidar Ratio (sr), Number of cases, Δ LR (upgraded - 44 sr)



505 **Figure 6: Geographical distribution of (a) the mean dust Lidar Ratio (LR), (b) the number of dust cases (N), and (c) the departures of the updated dust LR from the default value of 44 sr used in the CALIPSO retrieval algorithm, all derived from the CALIOP-MIDAS synergy for the period 2007–2017. The values are computed at each $2^\circ \times 5^\circ$ predefined grid. Grey-shaded grid cells indicate regions with only one available dust case, for which no robust LR estimate is provided.**

The spatial distribution of the dust LR uncertainties (Fig. 7) reveals that the LR retrieval uncertainty σ' (Fig. 7a) is the dominant contributor to the total uncertainty across most regions. Over the Central Sahara and Central Asian domains, σ' generally ranges between ~ 2 and 5 sr, leading to similarly low total uncertainties in Fig. 7c. In these regions, the standard error (SE; Fig. 7b) remains comparatively small, reflecting both limited case-by-case variability and the sufficient number of dust cases (Fig. 510 7b) used to derive the mean LR values. In contrast, the highest total uncertainties, locally reaching ~ 8 –11 sr (Fig. 7c), are observed over parts of the Central Asia (e.g., Iran). In these regions, the elevated total uncertainty primarily originates from the increased σ' values (Fig. 7a), indicating substantial retrieval uncertainty in the individual LR estimates. The SE component (Fig. 7b) also becomes significant in areas where only a few dust cases are available (e.g., 2–3 cases over parts of Iran), which

515 inflates the sampling-related uncertainty and contributes to the elevated total uncertainty. The enhanced uncertainties over
distinct parts of the Middle East may reflect the convergence of dust plumes from Saharan and Central Asian source regions
(Rezazadeh et al., 2013; Al-Hemoud et al., 2022; Gkikas et al., 2022), which promotes mixing between mineralogically distinct
dust types with different intrinsic lidar ratios (Caquineau et al., 2002; Scheuven et al., 2013; Ahmady-Birgani et al., 2019).
Additionally, potential aerosol-type misclassification in CALIPSO retrievals may contribute to the observed spread in LR. For
520 example, pollution over the Middle East or misclassified smoke layers transported from Central African biomass-burning
regions over the Sahel (Groß et al., 2011) may further enhance this variability.



525 **Figure 7: Geographical distribution of (a) the LR retrieval uncertainty σ' , (b) the standard error (SE) associated with the case-to-case variability of LR, and (c) the total LR uncertainty σ_{total} , all derived from the CALIOP-MIDAS synergy for the period 2007-2017. The values are computed at each $2^\circ \times 5^\circ$ predefined grid. Grey-shaded grid cells indicate regions with only one available dust case, for which no robust LR estimate is provided.**

The seasonal dust LR maps derived from the CALIOP–MIDAS synergy (Fig. 8) exhibit a broadly consistent spatial pattern throughout the year, with limited seasonal variability over most desert regions. In all seasons, the highest LR values (~52–60 sr) occur primarily over the Bodélé Depression and the Libyan Desert, two of the most intense and persistent dust sources of North Africa (Ginoux et al., 2012). Moderate LR values (~44–50 sr) dominate the remaining Saharan belt, the Central Asia and distinct regions of Arabian Peninsula, while the lowest values (~38–44 sr) appear over central parts of Arabian Peninsula and Sahel.

Despite the overall spatial stability, subtle seasonal differences are detected. During JJA, slightly enhanced LR values appear over parts of North Africa, consistent with the stronger dust mobilisation and long-range transport that characterise the summer period. Under the prevalence of strong surface winds and low-level jet streams, dust production and export from major source regions intensify (Al-Hemoud et al., 2022; Gkikas et al., 2022). Conversely, during DJF, dust production diminishes, with the dust LR hotspots restricted mainly over the major dust sources. During MAM and SON, the LR distribution shows a transitional pattern between the more active (JJA) and the less active seasons (DJF) for dust emission and transport. Moreover, the seasonal spatial patterns of dust LR deviations from the CALIOP default dust value of 44 sr (Δ LR; Fig. S6) offer direct insight into the regional validity of the fixed-LR assumption. The corresponding distributions of the seasonal uncertainties and the number of dust cases over each predefined grid (Figs. S7–S11) indicate that the magnitude of the seasonal LR uncertainties is largely controlled by the number of available CALIOP–MIDAS samples. Larger uncertainties appear in regions where only a few dust cases are available, while areas with more frequent dust detection—especially over the central Sahara—display lower uncertainties.

Overall, the combined analysis of the annual and seasonal dust LR maps, together with the corresponding number of cases, uncertainty estimates, and deviations from the default CALIOP dust LR (44 sr), shows that the regional variability of the dust LR is both statistically robust and physically consistent. The spatial patterns identified across North Africa, the Arabian Peninsula, and Central Asia highlight that dust optical properties differ substantially between major source regions and transport pathways. These synergistic satellite-based findings, together with ground-based lidar observations showing similar regional variability in dust lidar ratio (Müller et al., 2007; Groß et al., 2011; Preißler et al., 2011; Tesche et al., 2009, 2011; Kanitz et al., 2013; Baars et al., 2016; Rittmeister et al., 2017; Kaduk, 2017; Haarig et al., 2017a; Urbanneck, 2018; Bohlmann et al., 2018; Filioglou et al., 2020; Szczepanik et al., 2021; Haarig et al., 2022), provide strong support that the assumption of a globally constant dust LR of 44 sr is inadequate for representing the true spatial variability of dust optical properties. Instead, a regionally varying dust LR is required to achieve more accurate CALIOP-based dust retrievals.

Seasonal Dust Lidar Ratio distribution CALIOP-MIDAS [2007-2017]

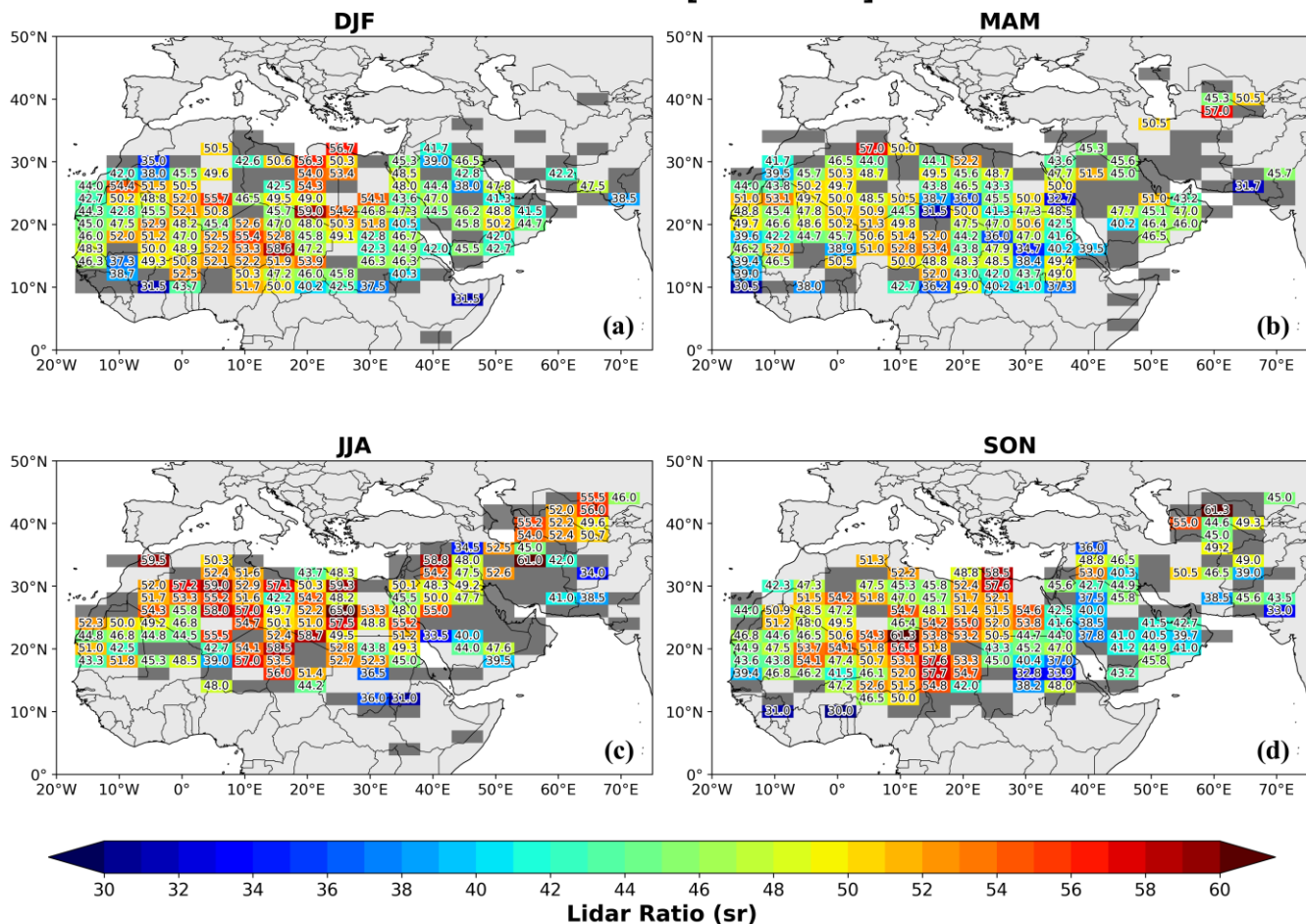


Figure 8: Seasonal geographical distributions of dust Lidar Ratio (LR) for (a) DJF, (b) MAM, (c) JJA and (d) SON resulted via the synergy CALIOP-MIDAS. The values represent the mean LR at each $2^\circ \times 5^\circ$ predefined grid. Grey-shaded grid cells indicate regions with only one available dust case, for which no robust LR estimate is provided.

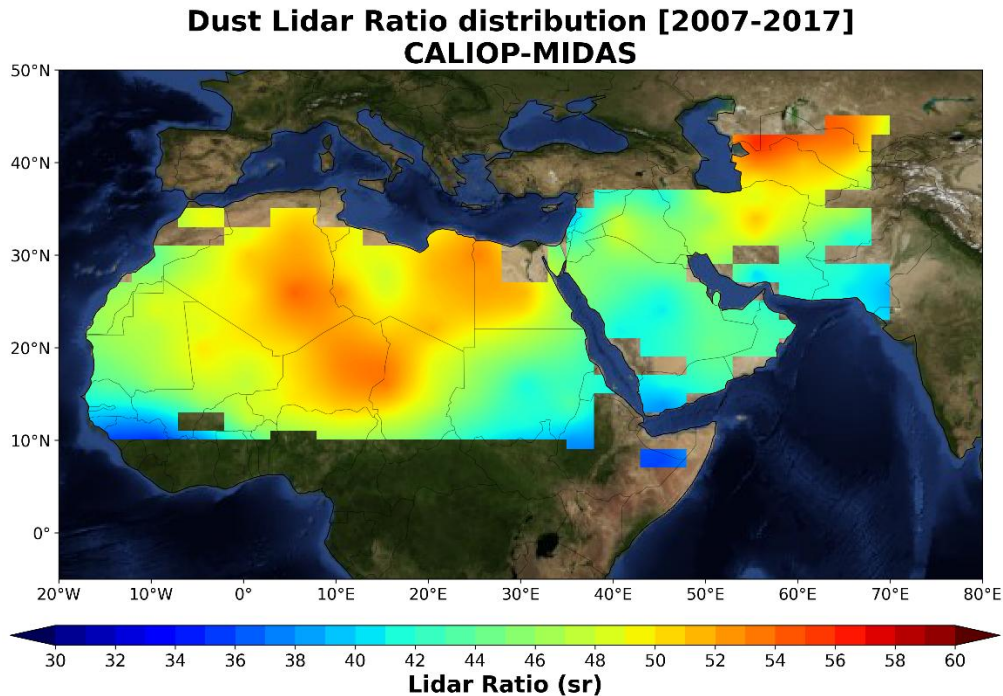
5 Summary and conclusions

The CALIPSO satellite mission has provided unprecedented state-of-the-art aerosol and cloud observations over a 17-year period (2006-2023), significantly improving our knowledge of various aerosol-related processes relevant to a wide range of environmental applications. The CALIOP lidar, mounted on the CALIPSO satellite, has delivered aerosol and cloud vertical profiles, up to the lower stratosphere, probing areas characterized by diverse atmospheric constituents. One of the key advantages of the CALIOP lidar is the deployment of a depolarization channel enabling the detection of non-spherical particles (e.g., dust, volcanic ash, ice crystals). Previous studies have documented that the CALIPSO aerosol retrieval algorithm outperforms when mineral dust particles are probed in the atmosphere. For the retrieval of the aerosol backscatter and

570 extinction coefficients with elastic lidars (such as CALIOP), the lidar ratio is needed as a-priori information. For dust aerosols,
the lidar ratio is set to 44 sr in the CALIPSO aerosol retrieval algorithm and is constant worldwide. However, ground-based
lidar measurements acquired at different places of the world have shown that the dust LR varies in space and time. Driven by
this fact, in the present study we focus on the estimation of the dust LRs over North Africa and Middle East, encompassing
the most active dust sources of the planet. Our analysis relies on a synergistic approach by combining CALIPSO vertical dust
575 profiles (a set of strict criteria has been implemented to ensure the presence of only mineral dust) with quality-assured columnar
passive aerosol retrievals derived from the MIDAS dataset (MODIS-based) and the POLDER-3/GRASP satellite observations.
All spaceborne instruments are/were part of the A-Train constellation thus enabling coincident observations. The study period
covers a 12-year period of CALIPSO overpasses, spanning from June 2006 to December 2017. We have calculated the updated
(revised) dust LRs at 532 nm within the study domain by collocating: (i) CALIOP-POLDER-3/GRASP during the period
580 2006-2009, (ii) CALIOP-MIDAS during the period 2007-2017 and (iii) CALIOP-MIDAS, on a seasonal basis, over the period
2007-2017.

The dust LR maps produced display a significant spatial variability over both North Africa and in the Middle East. According
to our findings, the highest dust LRs are recorded over and near the Bodélé Depression in the northern Chad basin (values up
to 56.2 sr), over the Libyan desert (~48–56 sr) and over dust-affected areas eastwards of the Caspian Sea (47–56 sr). Across
585 the Arabian Peninsula, the adjusted dust LR values exhibit pronounced spatial variability, with lower values (~38–45 sr) over
the central and southern regions and locally higher values (~46–54 sr) toward the northern Arabian Peninsula and
Mesopotamia; overall, most of these values remain at or below the default CALIPSO dust LR of 44 sr. For clarity, a spatially
smoothed representation of the dust LR map from CALIOP-MIDAS synergy is shown in Fig. 9, highlighting the dominant
regional patterns discussed above. Based on the CALIOP-MIDAS synergy on a seasonal basis, it is found that the highest dust
590 LRs are obtained in JJA, while the lowest ones are recorded in DJF, indicating that the proposed adjustments follow the dust
optical depth seasonal cycle. In addition to the dust LR maps, the estimated uncertainty fields further reinforce the robustness
of the retrieved regional patterns. Over the Central Sahara and Central Asian domains, the total LR uncertainties remain
relatively low (typically ~2–5 sr), reflecting both limited retrieval variability in the daily LR estimates and the sufficiently
large number of dust cases contributing to the grid-cell averages. In contrast, higher uncertainties—locally reaching ~8–11
595 sr—emerge primarily over parts of the Central Asia (e.g. Iran). These enhanced uncertainties arise from the combined effect
of larger retrieval uncertainties in these regions and the reduced number of cases, which amplifies the standard-error component
of the total uncertainty, particularly in locations where only 2–3 dust cases are available. Moreover, the elevated uncertainties
over selected Middle Eastern and Central Asian regions likely reflect the convergence of dust plumes from different source
regions and the resulting mixing of mineralogical distinct dust types, as well as potential aerosol-type misclassification in
600 CALIPSO retrievals. Similar effects may also arise over Sahel, where occasional misclassified smoke layers transported from
Central African biomass-burning areas can introduce additional variability in the retrieved LR values. Taken together, the
uncertainty patterns indicate that, while elevated uncertainties may influence the LR estimates in some regions, the broader
spatial differences identified in the dust LR maps are not primarily artifacts of retrieval noise or sampling limitations, but

605 instead reflect physically meaningful variability in dust optical properties across North Africa, the Middle East, and Central Asia.



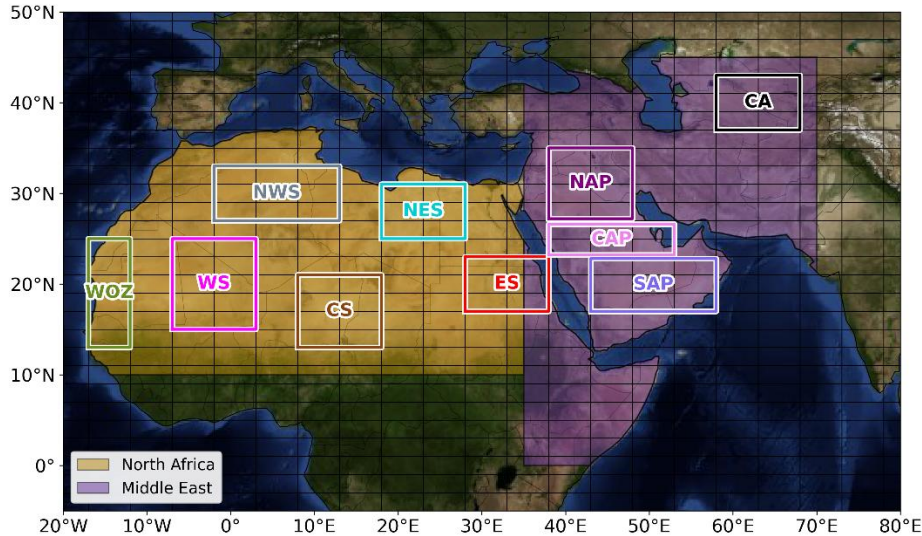
610 **Figure 9: Geographical distribution of the mean dust lidar ratio (LR) derived from the CALIOP–MIDAS synergy for the period 2007–2017. The underlying LR values are computed at each $2^\circ \times 5^\circ$ predefined grid cell, while a spatially smoothed representation is shown to emphasize large-scale regional patterns. Only grid cells with more than one dust case contribute to the displayed field. Map source: NASA Earth Observatory.**

The summary table of regional dust LR values (Table 2), estimated following Eq. (13), provides a compact overview of the spatial differences identified by the two CALIOP-based synergies across ten sub-regions defined within the broader desert domains (Fig. 10) over the most active and representative dust-producing areas. Over North Africa regions, the CALIOP–MIDAS and CALIOP–POLDER-3/GRASP synergies yield nearly identical regional LR values (typically 45–53 sr), underscoring the strong consistency between the two datasets across the major Saharan source regions. Across the broader Middle East domain, the regional dust LR values are relatively consistent, clustering around ~45 sr. Pronounced differences between the two synergistic approaches arise across the Arabian Peninsula. The CALIOP–POLDER-3/GRASP synergy lead to LR values greater than 44 sr across all Arabian sub-regions, whereas the CALIOP–MIDAS synergy yields somewhat lower values over the central and southern Peninsula. This discrepancy may partly reflect the much more limited temporal sampling of the CALIOP-POLDER-3/GRASP synergy (2006–2009), but also differences in sensor characteristics and retrieval assumptions. Importantly, the uncertainties associated with the CALIOP-POLDER-3/GRASP LR estimates are substantially larger—up to ~50% relative to CALIOP-MIDAS—such that the two synergistic approaches exhibit considerable overlap

625 within their uncertainty ranges. This suggests that, despite the apparent regional differences, the two datasets remain broadly consistent once retrieval uncertainty is taken into account.

Table 2: Summary of regional dust lidar ratio (LR) statistics at 532 nm derived from the two CALIOP-based synergies used in this study. The table reports the mean dust LR and its total uncertainty ($LR \pm \sigma$) for 10 desert subregions (defined in Fig. 10), separately for the CALIOP–MIDAS synergy (2007–2017) and the CALIOP–POLDER-3/GRASP synergy (2006–2009).

Regions	Geographical boundaries	Dust LR $\pm \sigma$ (sr)	
		CALIOP-MIDAS	CALIOP-POLDER-3/GRASP
North Africa		49.3 \pm 2.7	50.3 \pm 4.3
Central Sahara (CS)	13°–21° N, 8°–18° E	53.5 \pm 1.9	52.2 \pm 3.7
Northwestern Sahara (NWS)	27°–33° N, 2° W–13° E	50.8 \pm 3.3	51.2 \pm 5.4
Northeastern Sahara (NES)	25°–31° N, 18°–28° E	52.0 \pm 2.4	52.4 \pm 3.7
Western Sahara (WS)	15°–25° N, 7° W–3° E	49 \pm 2.0	49.7 \pm 3.5
Eastern Sahara (ES)	17°–23° N, 28°–38° E	45.6 \pm 2.5	48.6 \pm 3.6
Western Outflow Zone (WOZ)	13°–25° N, 17° W–12° W	45.5 \pm 2.6	45.7 \pm 3.5
Middle East		45.6 \pm 3.6	45.4 \pm 5.1
Northern Arabian Peninsula (NAP)	27.2°–35° N, 38°–48° E	47.8 \pm 3.1	46.3 \pm 3.6
Central Arabian Peninsula (CAP)	23.2°–26.6° N, 38°–53° E	43.3 \pm 4.3	48.1 \pm 5.5
Southern Arabian Peninsula (SAP)	17°–22.8° N, 43°–58° E	44.2 \pm 2.6	46.6 \pm 3.8
Central Asia (CA)	37°–43° N, 58°–68° E	50.2 \pm 3.3	48.1 \pm 5.3



630 **Figure 10: The spatial extent of the 10 sub-regions used in Table 2: Central Sahara (CS), Western Outflow Zone (WOZ), Northwestern Sahara (NWS), Northeastern Sahara (NES), Western Sahara (WS), Eastern Sahara (ES), Central Asia (CA), Northern Arabian Peninsula (NAP), Central Arabian Peninsula (CAP), and Southern Arabian Peninsula (SAP). Map source: NASA Earth Observatory.**

635 Our research aims to enhance the efficacy of CALIPSO dust retrievals, thereby increasing their utility in a broad range of
scientific studies. The analysis performed here can be extended to other major desert regions in the Northern Hemisphere (e.g.,
the Taklamakan Desert), as well as to the geographically more limited and less active dust source areas in the Southern
Hemisphere. Moreover, the proposed methodology is not restricted to dust: it can be readily applied to all CALIPSO aerosol
640 subtypes, such as marine aerosols, provided the analysis is focused on regions where different aerosol species dominate (e.g.,
clean marine over oceanic regions, polluted continental/smoke or elevated smoke over Central Africa, etc.). This flexibility
highlights the broader applicability of our approach for refining CALIPSO aerosol optical retrievals across diverse
environments. In a follow-up study, we will investigate the dust-induced direct radiative effects based on radiative transfer
model (RTM) simulations. This will involve the use of the updated CALIPSO dust profiles, the intensive spectral optical
properties (including single scattering albedo, asymmetry parameter, and refractive index) obtained by the GRASP/POLDER-
645 3 retrieval algorithm for the identified dust cases, along with the spectral surface albedos sourced from the HAMSTER dataset
(Rocchetti et al., 2024). Given the strong dependence of dust LRs on the composition of the mineral particles (Ansmann and
Müller, 2005; Gómez Maqueo Anaya et al., 2025; Li et al., 2025), the incorporation of the mineralogical maps derived by the
EMIT instrument (Connelly et al., 2021; Coleman et al., 2024) will strengthen the interpretation of the outcomes obtained in
the current study. A future assessment and validation of our findings will be possible through comparison with the vertically
650 resolved lidar ratio observations to be provided by the ATLID lidar onboard the EarthCARE satellite (Illingworth et al., 2015;
Wandinger et al., 2023; Wehr et al., 2023) or with the ACDL high-spectral-resolution lidar (HSRL) at 532 nm onboard the
DQ-1 satellite launched in April 2022 (Dai et al., 2024). Finally, one of the key updates in the forthcoming CALIPSO Version
5 retrieval algorithm involves the adoption of new aerosol models for lidar ratio estimation, further highlighting the need for
an improved and regionally representative characterization of this critical parameter.

655 *Data availability.* The LIVAS dust products are available upon request from Vassilis Amiridis (vamoir@noa.gr), Emmanouil
Proestakis (proestakis@noa.gr), and/or Eleni Marinou (elmarinou@noa.gr). The MIDAS dataset has been developed in the
framework of the DUST-GLASS project (grant no. 749461; European Union's Horizon 2020 research and innovation program
under the Marie Skłodowska-Curie Actions) and is available at <https://doi.org/10.5281/zenodo.4244106> (Gkikas et al., 2020).
The POLDER-3/GRASP Components products are publicly available at the GRASP-OPEN website ([https://www.grasp-
open.com/products/polder-data-release/](https://www.grasp-
660 open.com/products/polder-data-release/)). The Aerosol Robotic Network (AERONET) data are publicly available and can be
accessed through the official website at: <https://aeronet.gsfc.nasa.gov/>. The annual and seasonal gridded dust Lidar Ratio (LR)
dataset resulted via the different synergies (CALIOP-POLDER-3/GRASP and CALIOP-MIDAS) over North Africa and the

Middle East within the framework of this study is available at <https://doi.org/10.5281/zenodo.18016524> (Moustaka et al., 2025).

665 *Author contributions.* Conceptualization, A.M., N.S., A.G.; methodology, A.M., N.S., A.G., S.K., V.A.; software, A.M., N.S.; writing—original draft preparation, A.M.; writing—review and editing, A.M., A.G., N.S., K.A.V., E.P., A.L., S.K., O.D., K.T., C.Z., V.A.; funding acquisition, A.G., S.K. All authors have read and agreed to the published version of the manuscript.

670 *Financial support.* This work was supported both from COST Action CA21119 Harmonia: International network for harmonisation of atmospheric aerosol retrievals from ground based photometers, supported by COST (European Cooperation in Science and Technology) and the Hellenic Foundation for Research and Innovation (H.F.R.I.) under the “2nd Call for H.F.R.I. Research Projects to support Post-Doctoral Researchers” (Project Number: 544)

675 *Acknowledgment.* We want to acknowledge the use of POLDER data "POLDER/PARASOL Level-1 data originally provided by CNES (<http://www.icare.univ-lille1.fr/>) and AERIS/ICARE Data and Services Center, processed by Cloudflight Austria GmbH with GRASP software (<https://www.grasp-open.com>) developed by Dubovik et al. (2011, 2014, 2021) and Li et al. (2019). This study benefited from contributions made within the AIRSENSE (Aerosol and aerosol cloud Interaction from Remote SENSing Enhancement) project, funded by the European Space Agency under Contract No. 4000142902/23/I-NS. This project also received funding from the European Union’s Horizon 2020 research and innovation programme under grant agreement No. 871115. ACTRIS-D is funded by the German Federal Ministry for Education and Research (BMBF) under grant agreements 01LK2001A-K and 01LK2002A-G. Stelios Kazadzis, would like to acknowledge the ACTRIS Switzerland 680 2025–2028 grant (Swiss contribution to the ACTRIS ERIC) funded by the Swiss State Secretariat for Education and Research and Innovation (SERI).

Competing interests. Some authors are members of the editorial board of AMT.

Disclaimer.

Special issue statement.

685 **References**

- Ahmady-Birgani, H., Engelbrecht, J. P., and Bazgir, M.: How different source regions across the Middle East change aerosol and dust particle characteristics, *Desert*, 24, 61-73, doi:10.22059/jdesert.2019.72441, 2019.
- Al-Hemoud, A., Al-Dashti, H., Al-Saleh, A., Petrov, P., Malek, M., Elhamoud, E., Karam, R., Al-Khatib, L., Alyahya, M., Al-Azemi, H., Al-Mutairi, N., Moulton, J., and Middleton, N.: Dust storm ‘hot spots’ and transport pathways affecting the Arabian Peninsula. *Journal of Atmospheric and Solar-Terrestrial Physics*, 238, 105932, doi:10.1016/j.jastp.2022.105932, 2022.
- 690 Althausen, D., Abdullaev, S., and Hofer, J.: Scientists share results of dust belt research, *EOS, Science News by AGU*, 100, doi:10.1029/2019EO131683, 2019.

- Amiridis, V., Marinou, E., Tsekeri, A., Wandinger, U., Schwarz, A., Giannakaki, E., Mamouri, R., Kokkalis, P., Biniotoglou, I., Solomos, S., Herekakis, T., Kazadzis, S., Gerasopoulos, E., Proestakis, E., Kottas, M., Balis, D., Papayannis, A., Kontoes, C., Kourtidis, K., Papagiannopoulos, N., Mona, L., Pappalardo, G., Le Rille, O., and Ansmann, A.: LIVAS: a 3-D multi-wavelength aerosol/cloud database based on CALIPSO and EARLINET, *Atmos. Chem. Phys.*, 15, 7127–7153, doi:10.5194/acp-15-7127-2015, 2015.
- Anderson, T. L., Wu, Y., Chu, D. A., Schmid, B., Redemann, J., and Dubovik, O.: Testing the MODIS satellite retrieval of aerosol fine-mode fraction, *J. Geophys. Res.*, 110, D18204, doi:10.1029/2005JD005978, 2005.
- 695 Ångström, A.: On the atmospheric transmission of Sun radiation and on dust in the air, *Geogr. Ann.*, 11, 156–166, doi:10.2307/519399, 1929.
- Ansmann, A. and Müller, D.: Lidar and atmospheric aerosol particles, in: *Lidar–Range-Resolved Optical Remote Sensing of the Atmosphere*, vol. 102 of Springer Series in Optical Sciences, edited by: Weitkamp, C., Springer, Berlin, Heidelberg, 105–141, 2005.
- 705 Ansmann, A., Petzold, A., Kandler, K., Tegen, I., Wendisch, M., Müller, D., Weinzierl, B., Müller, T., and Heintzenberg, J.: Saharan Mineral Dust Experiments SAMUM–1 and SAMUM–2: what have we learned?, *Tellus B*, 63, 403–429, doi:10.1111/j.1600-0889.2011.00555.x, 2011.
- Baars, H., Kanitz, T., Engelmann, R., Althausen, D., Heese, B., Komppula, M., Preissler, J., Tesche, M., Ansmann, A., Wandinger, U., Lim, J. H., Ahn, J. Y., Stachlewska, I. S., Amiridis, V., Marinou, E., Seifert, P., Hofer, J., Skupin, A., 710 Schneider, F., Bohlmann, S., Foth, A., Bley, S., Pfuller, A., Giannakaki, E., Lihavainen, H., Viisanen, Y., Hooda, R. K., Pereira, S. N., Bortoli, D., Wagner, F., Mattis, I., Janicka, L., Markowicz, K. M., Achtert, P., Artaxo, P., Pauliquevis, T., Souza, R. A. F., Sharma, V. P., van Zyl, P. G., Beukes, J. P., Sun, J. Y., Rohwer, E. G., Deng, R. R., Mamouri, R. E., and Zamorano, F.: An overview of the first decade of Polly(NET): an emerging network of automated Raman-polarization lidars for continuous aerosol profiling, *Atmos. Chem. Phys.*, 16, 5111–5137, doi:10.5194/acp-16-5111-2016, 2016.
- 715 Banks, J. R., Heinold, B., and Schepanski, K.: Impacts of the desiccation of the Aral Sea on the Central Asian dust life-cycle. *J. Geophys. Res.: Atmos.*, 127, doi:10.1029/2022JD036618, 2022.
- Benkhalifa, J., Leon, J. F., and Chaabane, M.: Aerosol optical properties of Western Mediterranean basin from multi-year AERONET data, *J. Atmos. Sol.-Terr. Phys.*, 164, 222–228, doi:10.1016/j.jastp.2017.08.029, 2017.
- Bohlmann, S., Baars, H., Radenz, M., Engelmann, R., and Macke, A.: Ship-borne aerosol profiling with lidar over the Atlantic 720 Ocean: from pure marine conditions to complex dust–smoke mixtures, *Atmos. Chem. Phys.*, 18, 9661–9679, doi:10.5194/acp-18-9661-2018, 2018.
- Burton, S. P., Ferrare, R. A., Hostetler, C. A., Hair, J. W., Rogers, R. R., Obland, M. D., Butler, C. F., Cook, A. L., Harper, D. B., and Froyd, K. D.: Aerosol classification using airborne High Spectral Resolution Lidar measurements – methodology and examples, *Atmos. Meas. Tech.*, 5, 73–98, doi:10.5194/amt-5-73-2012, 2012.

- 725 Burton, S. P., Ferrare, R. A., Vaughan, M. A., Omar, A. H., Rogers, R. R., Hostetler, C. A., and Hair, J. W.: Aerosol classification from airborne HSRL and comparisons with the CALIPSO vertical feature mask, *Atmos. Meas. Tech.*, 6, 1397–1412, doi:10.5194/amt-6-1397-2013, 2013.
- Caquineau, S., Gaudichet, A., Gomes, L., and Legrand, M.: Mineralogy of Saharan dust transported over northwestern tropical Atlantic Ocean in relation to source regions, *J. Geophys. Res.*, 107, 4251, doi:10.1029/2000jd000247, 2002.
- 730 Castellanos, P., Colarco, P., Espinosa, W. R., Guzewich, S. D., Levy, R. C., Miller, R. L., Chin, M., Kahn, R. A., Kemppinen, O., Moosmüller, H., Nowottnick, E. P., Rocha-Lima, A., Smith, M. D., Yorks, J. E., and Yu, H.: Mineral dust optical properties for remote sensing and global modeling: A review, *Remote Sens. Environ.*, 303, 113982, doi:10.1016/j.rse.2023.113982, 2024.
- Chen, C., Dubovik, O., Fuertes, D., Litvinov, P., Lapyonok, T., Lopatin, A., Ducos, F., Derimian, Y., Herman, M., Tanré, D., Remer, L. A., Lyapustin, A., Sayer, A. M., Levy, R. C., Hsu, N. C., Descloitres, J., Li, L., Torres, B., Karol, Y., Herrera, M.,
- 735 Herreras, M., Aspetsberger, M., Wanzenboeck, M., Bindreiter, L., Marth, D., Hangler, A., and Federspiel, C.: Validation of GRASP algorithm product from POLDER/PARASOL data and assessment of multi-angular polarimetry potential for aerosol monitoring, *Earth Syst. Sci. Data*, 12, 3573–3620, doi:10.5194/essd-12-3573-2020, 2020.
- Chen, S., Jiang, N., Huang, J., Xu, X., Zhang, H., Zang, Z., Huang, K., Xu, X., Wei, Y., Guan, X., Zhang, X., Luo, Y., Hu, Z., and Feng, T.: Quantifying contributions of natural and anthropogenic dust emission from different climatic regions, *Atmos. Environ.*, 191, 94–104, doi:10.1016/j.atmosenv.2018.07.043, 2018.
- 740 Cole, J. N. S., Barker, H. W., Qu, Z., Villefranque, N., and Shephard, M. W.: Broadband radiative quantities for the EarthCARE mission: the ACM-COM and ACM-RT products, *Atmos. Meas. Tech.*, 16, 4271–4288, doi:10.5194/amt-16-4271-2023, 2023.
- Coleman, R. W., Thompson, D. R., Brodrick, P. G., Dor, E. B., Cox, E., García-Pando, C. P., Hoefen, T., Kokaly, R. F., Meyer, J. M., Ochoa, F., Okin, G. S., Pearlshien, D. H., Swayze, G., and Green, R. O.: An accuracy assessment of the surface reflectance product from the EMIT imaging spectrometer, *Remote Sens. Environ.*, 315, 114450, doi:10.1016/j.rse.2024.114450, 2024.
- 745 Connelly, D. S., Thompson, D. R., Mahowald, N. M., Li, L., Carmon, N., Okin, G. S., and Green, R. O.: The EMIT mission information yield for mineral dust radiative forcing, *Remote Sens. Environ.*, 258, 112380, doi:10.1016/j.rse.2021.112380, 2021.
- 750 Deshler, T., Johnson, B. J., and Rozier, W. R.: Balloonborne measurements of Pinatubo aerosol during 1991 and 1992 at 41° N: vertical profiles, size distribution, and volatility, *Geophys. Res. Lett.*, 20, 1435–1438, doi:10.1029/93GL01337, 1993.
- Dubovik, O., Sinyuk, A., Lapyonok, T., Holben, B. N., Mishchenko, M., Yang, P., Eck, T. F., Volten, H., Muñoz, O., Veihelmann, B., van der Zande, W. J., Leon, J. F., Sorokin, M., and Slutsker, I.: Application of spheroid models to account for aerosol particle nonsphericity in remote sensing of desert dust, *J. Geophys. Res.-Atmos.*, 111, 1–34, doi:10.1029/2005JD006619, 2006.
- 755 Dubovik, O., Herman, M., Holdak, A., Lapyonok, T., Tanré, D., Deuzé, J. L., Ducos, F., Sinyuk, A., and Lopatin, A.: Statistically optimized inversion algorithm for enhanced retrieval of aerosol properties from spectral multi-angle polarimetric satellite observations, *Atmos. Meas. Tech.*, 4, 975–1018, doi:10.5194/amt-4-975-2011, 2011.

- Dubovik, O., Schuster, G. L., Xu, F., Hu, Y., Bösch, H., Landgraf, J., and Li, Z.: Grand Challenges in Satellite Remote Sensing, *Front. Remote Sens.*, 2, 1–10, doi:10.3389/frsen.2021.619818, 2021.
- Engelstaedter, S., Tegen, I., and Washington, R.: North African dust emissions and transport, *Earth-Sci. Rev.*, 79, 73–100, doi:10.1016/j.earscirev.2006.06.004, 2007.
- Filioglou, M., Giannakaki, E., Backman, J., Kesti, J., Hirsikko, A., Engelmann, R., O'Connor, E., Leskinen, J. T. T., Shang, X., Korhonen, H., Lihavainen, H., Romakkaniemi, S., and Komppula, M.: Optical and geometrical aerosol particle properties over the United Arab Emirates, *Atmos. Chem. Phys.*, 20, 8909–8922, doi:10.5194/acp-20-8909-2020, 2020.
- Floutsi, A. A., Baars, H., Engelmann, R., Althausen, D., Ansmann, A., Bohlmann, S., Heese, B., Hofer, J., Kanitz, T., Haarig, M., Ohneiser, K., Radenz, M., Seifert, P., Skupin, A., Yin, Z., Abdullaev, S. F., Komppula, M., Filioglou, M., Giannakaki, E., Stachlewska, I. S., Janicka, L., Bortoli, D., Marinou, E., Amiridis, V., Gialitaki, A., Mamouri, R.-E., Barja, B., and Wandinger, U.: DeLiAn – a growing collection of depolarization ratio, lidar ratio and Ångström exponent for different aerosol types and mixtures from ground-based lidar observations, *Atmos. Meas. Tech.*, 16, 2353–2379, doi:10.5194/amt-16-2353-2023, 2023.
- Fountoulakis, I., Kosmopoulos, P., Papachristopoulou, K., Raptis, I.-P., Mamouri, R.-E., Nisantzi, A., Gkikas, A., Witthuhn, J., Bley, S., Moustaka, A., Buehl, J., Seifert, P., Hadjimitsis, D., Kontoes, C., and Kazadzis, S.: Effects of Aerosols and Clouds on the Levels of Surface Solar Radiation and Solar Energy in Cyprus, *Remote Sens.*, 13, 2319, doi:10.3390/rs13122319, 2021.
- Fountoulakis, I., Papachristopoulou, K., Proestakis, E., Amiridis, V., Kontoes, C., and Kazadzis, S.: Effect of Aerosol Vertical Distribution on the Modeling of Solar Radiation, *Remote Sensing*, 14, 1143, doi:10.3390/rs14051143, 2022.
- Freudenthaler, V., Esselborn, M., Wiegner, M., Heese, B., Tesche, M., Ansmann, A., Müller, D., Althausen, D., Wirth, M., Fix, A., Ehret, G., Knippertz, P., Toledano, C., Gasteiger, J., Garhammer, M., and Seefeldner, M.: Depolarization ratio profiling at several wavelengths in pure Saharan dust during SAMUM 2006, *Tellus B*, 61, 165–179, doi:10.1111/j.16000889.2008.00396.x, 2009.
- Ge, J. M., Huang, J. P., Xu, C. P., Qi, Y. L., and Liu, H. Y.: Characteristics of Taklimakan dust emission and distribution: a satellite and reanalysis field perspective, *J. Geophys. Res.-Atmos.*, 119, 11772–11783, doi:10.1002/2014JD022280, 2014.
- Gelaro, R., McCarty, W., Suárez, M. J., Todling, R., Molod, A., Takacs, L., Randles, C. A., Darmenov, A., Bosilovich, M. G., Reichle, R., Wargan, K., Coy, L., Cullather, R., Draper, C., Akella, S., Buchard, V., Conaty, A., da Silva, A. M., Gu, W., Kim, G.-K., Koster, R., Lucchesi, R., Merkova, D., Nielsen, J. E., Partyka, G., Pawson, S., Putman, W., Rienecker, M., Schubert, S. D., Sienkiewicz, M., and Zhao, B.: The modern-era retrospective analysis for research and applications, version 2 (MERRA-2), *Journal of Climate*, 30(14), 5419–5454, doi:10.1175/JCLI-D-16-0758.1, 2017.
- Giles, D. M., Sinyuk, A., Sorokin, M. G., Schafer, J. S., Smirnov, A., Slutsker, I., Eck, T. F., Holben, B. N., Lewis, J. R., Campbell, J. R., Welton, E. J., Korkin, S. V., and Lyapustin, A. I.: Advancements in the Aerosol Robotic Network (AERONET) Version 3 database – automated near-real-time quality control algorithm with improved cloud screening for Sun photometer aerosol optical depth (AOD) measurements, *Atmos. Meas. Tech.*, 12, 169–209, doi:10.5194/amt-12-169-2019, 2019.

- Ginoux, P., Prospero, J. M., Gill, T. E., Hsu, N. C., and Zhao, M.: Global-scale attribution of anthropogenic and natural dust sources and their emission rates based on MODIS Deep Blue aerosol products, *Rev. Geophys.*, 50, RG3005, doi:10.1029/2012RG000388, 2012.
- 795 Gkikas, A., Proestakis, E., Amiridis, V., Kazadzis, S., Di Tomaso, E., Tsekeri, A., Marinou, E., Hatzianastassiou, N., and Pérez García-Pando, C.: ModIs Dust AeroSol (MIDAS): A global fine resolution dust optical depth dataset, Zenodo, doi:10.5281/zenodo.4244106, 2020.
- Gkikas, A., Proestakis, E., Amiridis, V., Kazadzis, S., Di Tomaso, E., Tsekeri, A., Marinou, E., Hatzianastassiou, N., and Pérez García-Pando, C.: ModIs Dust AeroSol (MIDAS): a global fine-resolution dust optical depth data set, *Atmos. Meas. Tech.*,
800 14, 309–334, doi:10.5194/amt-14-309-2021, 2021.
- Gkikas, A., Proestakis, E., Amiridis, V., Kazadzis, S., Di Tomaso, E., Marinou, E., Hatzianastassiou, N., Kok, J. F., and García-Pando, C. P.: Quantification of the dust optical depth across spatiotemporal scales with the MIDAS global dataset (2003–2017), *Atmos. Chem. Phys.*, 22, 3553–3578, doi:10.5194/acp-22-3553-2022, 2022.
- Gómez Maqueo Anaya, S., Althausen, D., Hofer, J., Haarig, M., Wandinger, U., Heinold, B., Tegen, I., Faust, M., Baars, H.,
805 Ansmann, A., Engelmann, R., Skupin, A., Heese, B., and Schepanski, K.: Investigating the link between mineral dust hematite content and intensive optical properties by means of lidar measurements and aerosol modeling, *Atmos. Chem. Phys.*, 25, 9737–9764, doi:10.5194/acp-25-9737-2025, 2025.
- González-Romero, A., González-Flórez, C., Panta, A., Yus-Díez, J., Reche, C., Córdoba, P., Moreno, N., Alastuey, A., Kandler, K., Klose, M., Baldo, C., Clark, R. N., Shi, Z., Querol, X., and Pérez García-Pando, C.: Variability in sediment
810 particle size, mineralogy, and Fe mode of occurrence across dust-source inland drainage basins: the case of the lower Drâa Valley, Morocco, *Atmos. Chem. Phys.*, 23, 15815–15834, doi:10.5194/acp-23-15815-2023, 2023.
- Groß, S., Tesche, M., Freudenthaler, V., Toledano, C., Wiegner, M., Ansmann, A., Althausen, D., and Seefeldner, M.: Characterization of Saharan dust, marine aerosols and mixtures of biomass-burning aerosols and dust by means of multi-wavelength depolarization and Raman lidar measurements during SAMUM–2, *Tellus B*, 63, 706–724, doi:10.1111/j.1600-
815 0889.2011.00556.x, 2011.
- Groß, S., Freudenthaler, V., Schepanski, K., Toledano, C., Schäfler, A., Ansmann, A., and Weinzierl, B.: Optical properties of long-range transported Saharan dust over Barbados as measured by dual-wavelength depolarization Raman lidar measurements, *Atmospheric Chemistry and Physics*, 15(19), 11067–11080, doi:10.5194/acp-15-11067-2015, 2015.
- Gui, L., Tao, M., Wang, Y., Wang, L., Chen, L., Lin, C., Tao, J., Wang, J., and Yu, C.: Climatology of aerosol types and their
820 vertical distribution over East Asia based on CALIPSO lidar measurements. *Int. J. Climatol.*, 42, 6042–6054, doi:10.1002/joc.7599, 2022.
- Gupta, P., Remer, L.A., Patadia, F., Levy, R.C., and Christopher, S.A.: High-resolution gridded level 3 aerosol optical depth data from MODIS. *Remote Sens.*, 12, 2847, doi:10.3390/rs12172847, 2020.
- Haarig, M., Ansmann, A., Althausen, D., Klepel, A., Groß, S., Freudenthaler, V., Toledano, C., Mamouri, R.-E., Farrell, D.
825 A., Prescod, D. A., Marinou, E., Burton, S. P., Gasteiger, J., Engelmann, R., and Baars, H.: Triple-wavelength depolarization-

- ratio profiling of Saharan dust over Barbados during SALTRACE in 2013 and 2014, *Atmos. Chem. Phys.*, 17, 10767–10794, doi:10.5194/acp-17-10767-2017, 2017a.
- Haarig, M., Ansmann, A., Gasteiger, J., Kandler, K., Althausen, D., Baars, H., Radenz, M., and Farrell, D. A.: Dry versus wet marine particle optical properties: RH dependence of depolarization ratio, backscatter, and extinction from multiwavelength lidar measurements during SALTRACE, *Atmos. Chem. Phys.*, 17, 14199–14217, doi:10.5194/acp-17-14199-2017, 2017b.
- 830 Haarig, M., Ansmann, A., Baars, H., Jimenez, C., Veselovskii, I., Engelmann, R., and Althausen, D.: Depolarization and lidar ratios at 355, 532, and 1064 nm and microphysical properties of aged tropospheric and stratospheric Canadian wildfire smoke, *Atmos. Chem. Phys.*, 18, 11847–11861, doi:10.5194/acp-18-11847-2018, 2018.
- Haarig, M., Ansmann, A., Engelmann, R., Baars, H., Toledano, C., Torres, B., Althausen, D., Radenz, M., and Wandinger, U.: First triple wavelength lidar observations of depolarization and extinction-to-backscatter ratios of Saharan dust, *Atmos. Chem. Phys.*, 22, 355–369, doi:10.5194/acp-22-355-2022, 2022.
- 835 Hamidi, M., Kavianpour, M. R., and Shao, Y.: Synoptic analysis of dust storms in the Middle East, Asia-Pacific, *J. Atmos. Sci.*, 49, 279–286, doi:10.1007/s13143-013-0027-9, 2013.
- Hansen, J., Rossow, W., Carlson, B., Lacis, A., Travis, L., Del Genio, A., Fung, I., Cairns, B., Mishchenko, M., and Sato, M.: Low-cost long-term monitoring of global climate forcings and feedbacks, *Climatic Change*, 31, 247–271, doi:10.1007/BF01095149, 1995.
- 840 Hofer, J., Ansmann, A., Althausen, D., Engelmann, R., Baars, H., Fomba, K. W., Wandinger, U., Abdullaev, S. F., and Makhmudov, A. N.: Optical properties of Central Asian aerosol relevant for spaceborne lidar applications and aerosol typing at 355 and 532 nm, *Atmospheric Chemistry and Physics*, 20(15), 9265–9280, doi:10.5194/acp-20-9265-2020, 2020.
- 845 Holben, B. N., Eck, T. F., Slutsker, I., Tanré, D., Buis, J. P., Setzer, A., Vermote, E., Reagan, J. A., Kaufman, Y., Nakajima, T., Lavenue, F., Jankowiak, I., and Smirnov, A.: AERONET— A federated instrument network and data archive for aerosol characterization, *Remote Sens. Environ.*, 66, 1–16, doi:10.1016/S0034-4257(98)00031-5, 1998.
- Holben, B. N., Tanre, D., Smirnov, A., Eck, T. F., Slutsker, I., Abuhassan, N., Newcomb, W. W., Schafer, J., Chatenet, B., Lavenue, F., Kaufman, Y., Vande Castle, J., Setzer, A., Markham, B., Clark, D., Frouin, R., Halthore, R., Karnieli, A., O'Neill, N. T., Pietras, C., Pinker, R. T., Voss, K., and Zibordi, G.: An emerging ground-based aerosol climatology: Aerosol optical depth from AERONET, *J. Geophys. Res.*, 106, 12067–12097, doi:10.1029/2001JD900014, 2001.
- 850 Hu, Y., Winker, D., Vaughan, M., Lin, B., Omar, A., Trepte, C., Flittner, D., Yang, P., Sun, W., Liu, Z., Wang, Z., Young, S., Stamnes, K., Huang, J., Kuehn, R., Baum, B., and Holz, R.: CALIPSO/CALIOP Cloud Phase Discrimination Algorithm, *J. Atmos. Ocean. Tech.*, 26, 2293–2309, doi:10.1175/2009JTECHA1280.1, 2009.
- 855 Hu, Z., Huang, J., Zhao, C., Bi, J., Jin, Q., Qian, Y., Leung, L. R., Feng, T., Chen, S., and Ma, J.: Modeling the contributions of Northern Hemisphere dust sources to dust outflow from East Asia, *Atmos. Environ.*, 202, 234–243, doi:10.1016/j.atmosenv.2019.01.022, 2019.
- Huang, J. P., Wang, T. H., Wang, W. C., Li, Z. Q., and Yan, H. R.: Climate effects of dust aerosols over East Asian arid and semiarid regions, *J. Geophys. Res.-Atmos.*, 119, 11398–11416, doi:10.1002/2014JD021796, 2014.

- 860 Hyer, E. J., Reid, J. S., and Zhang, J.: An over-land aerosol optical depth data set for data assimilation by filtering, correction, and aggregation of MODIS Collection 5 optical depth retrievals, *Atmos. Meas. Tech.*, 4, 379–408, doi:10.5194/amt-4-379-2011, 2011.
- Illingworth, A. J., Barker, H. W., Beljaars, A., Ceccaldi, M., Chepfer, H., Cierbaux, N., Cole, J., Delanoë, J., Domenech, C., Donovan, D. P., Fukuda, S., Hirakata, M., Hogan, R. J., Huenerbein, A., Kolias, P., Kubota, T., Nakajima, T. Y., Nishizawa, T., Ohno, Y., Okamoto, H., Oki, R., Sato, K., Satoh, M., Shepherd, M. W., Velazques-Blazquez, A., Wandinger, U., Wehr, T., and van Zadelhoff, G.-J.: The EarthCARE satellite: The next step forward in global measurements of clouds, aerosols, precipitation, and radiation, *B. Am. Meteorol. Soc.*, 96, 1311–1332, doi:10.1175/BAMS-D-12-00227.1, 2015.
- 865 Jish Prakash, P., Stenchikov, G., Kalenderski, S., Osipov, S., and Bangalath, H.: The impact of dust storms on the Arabian Peninsula and the Red Sea, *Atmos. Chem. Phys.*, 15, 199–222, doi:10.5194/acp-15-199-2015, 2015.
- 870 Kaduk, C.: Characterization of the optical properties of complex aerosol mixtures observed with a multiwavelength–Raman polarization lidar during the 6-weeks BACCHUS campaign in Cyprus in spring 2015, MSc thesis, Leipzig University, https://www.tropos.de/fileadmin/user_upload/Institut/Abteilungen/Fernerkundung/Daten_PDF/MA_Clara_Kaduk.pdf (last access: 12 December 2024), 2017.
- Kang, E., Park, S., Kim, M., Yoo, C., Im, J., Song, C. K.: Direct aerosol optical depth retrievals using MODIS reflectance data and machine learning over East Asia. *Atmos. Environ.*, 309, 119951, doi:10.1016/j.atmosenv.2023.119951, 2023.
- 875 Kanitz, T., Ansmann, A., Engelmann, R., and Althausen, D.: North-south cross sections of the vertical aerosol distribution over the Atlantic Ocean from multiwavelength Raman/polarization lidar during Polarstern cruises, *J. Geophys. Res.-Atmos.*, 118, 2643–2655, doi:10.1002/jgrd.50273, 2013.
- Kim, M.-H., Kim, S.-W., and Omar, A. H.: Dust Lidar Ratios Retrieved from the CALIOP Measurements Using the MODIS AOD as a Constraint, *Remote Sens.*, 12, 251, doi:10.3390/rs12020251, 2020.
- 880 Kim, M.-H., Omar, A. H., Tackett, J. L., Vaughan, M. A., Winker, D. M., Trepte, C. R., Hu, Y., Liu, Z., Poole, L. R., Pitts, M. C., Kar, J., and Magill, B. E.: The CALIPSO version 4 automated aerosol classification and lidar ratio selection algorithm, *Atmos. Meas. Tech.*, 11, 6107–6135, doi:10.5194/amt-11-6107-2018, 2018.
- Kiriakidis, P., Gkikas, A., Papangelis, G., Christoudias, T., Kushta, J., Proestakis, E., Kampouri, A., Marinou, E., Drakaki, E., Benedetti, A., Rennie, M., Retscher, C., Straume, A. G., Dandocsi, A., Sciare, J., and Amiridis, V.: The impact of using assimilated Aeolus wind data on regional WRF-Chem dust simulations, *Atmos. Chem. Phys.*, 23, 4391–4417, doi:10.5194/acp-23-4391-2023, 2023.
- 885 Kok, J. F., Ridley, D. A., Zhou, Q., Miller, R. L., Zhao, C., Heald, C. L., Ward, D. S., Albani, S., and Haustein, K.: Smaller desert dust cooling effect estimated from analysis of dust size and abundance, *Nat. Geosci.*, 10, 274–278, doi:10.1038/ngeo2912, 2017.
- 890 Kok, J. F., Adebisi, A. A., Albani, S., Balkanski, Y., Checa-Garcia, R., Chin, M., Colarco, P. R., Hamilton, D. S., Huang, Y., Ito, A., Klose, M., Li, L., Mahowald, N. M., Miller, R. L., Obiso, V., Pérez García-Pando, C., Rocha-Lima, A., and Wan, J.

- S.: Contribution of the world's main dust source regions to the global cycle of desert dust, *Atmos. Chem. Phys.*, 21, 8169–8193, doi:10.5194/acp-21-8169-2021, 2021.
- 895 Kok, J. F., Storelvmo, T., Karydis, V. A., Adebisi, A. A., Mahowald, N. M., Evan, A. T., He, C., and Leung, D. M.: Mineral dust aerosol impacts on global climate and climate change, *Nat. Rev. Earth Environ.*, 4, 71–86, doi:10.1038/s43017022-00379-5, 2023.
- Konsta, D., Biniotoglou, I., Gkikas, A., Solomos, S., Marinou, E., Proestakis, E., Basart, S., Pérez García-Pando, C., El-Askary, H., and Amiridis, V.: Evaluation of the BSC-DREAM8b regional dust model using the 3D LIVAS-CALIPSO product, *Atmos. Environ.*, 195, 46–62, doi:10.1016/j.atmosenv.2018.09.047, 2018.
- 900 Li, D., Zhang, Y., Saito, M., Yang, P., and Hu, Y.: The impact of dust mineralogical compositions on CALIOP-IIR-based retrievals of the optical and microphysical properties of dust plumes, *J. Geophys. Res. Atmos.*, 130, doi:10.1029/2025JD043829, 2025.
- Li, L. and Sokolik, I.: Analysis of Dust Aerosol Retrievals Using Satellite Data in Central Asia, *Atmosphere*, 9, 288, doi:10.3390/atmos9080288, 2018.
- 905 Li, L., Dubovik, O., Derimian, Y., Schuster, G. L., Lapyonok, T., Litvinov, P., Ducos, F., Fuertes, D., Chen, C., Li, Z., Lopatin, A., Torres, B., and Che, H.: Retrieval of aerosol components directly from satellite and ground-based measurements, *Atmos. Chem. Phys.*, 19, 13409–13443, doi:10.5194/acp-19-13409-2019, 2019.
- Logothetis, S.-A., Salamalikis, V., Gkikas, A., Kazadzis, S., Amiridis, V., and Kazantzidis, A.: 15-year variability of desert dust optical depth on global and regional scales, *Atmos. Chem. Phys.*, 21, 16499–16529, doi:10.5194/acp-21-16499-2021, 2021.
- 910 Luo, Y., Zheng, X., and Chen, J.: A climatology of aerosol optical depth over China from recent 10 years of MODIS remote sensing data, *Int. J. Climatol.*, 34, 863–870, doi:10.1002/joc.3728, 2014.
- Ma, X., Bartlett, K., Harmon, K., and Yu, F.: Comparison of AOD between CALIPSO and MODIS: significant differences over major dust and biomass burning regions, *Atmos. Meas. Tech.*, 6, 2391–2401, doi:10.5194/amt-6-2391-2013, 2013.
- 915 Mahowald, N., Albani, S., Kok, J. F., Engelstaeder, S., Scanza, R., Ward, D. S., and Flanner, M. G.: The size distribution of desert dust aerosols and its impact on the Earth system, *Aeolian Res.*, 15, 53–71, doi:10.1016/j.aeolia.2013.09.002, 2014.
- Mao, K. B., Ma, Y., Xia, L., Chen, W. Y., Shen, X. Y., He, T. J., and Xu, T. R.: Global aerosol change in the last decade: An analysis based on MODIS data, *Atmos. Environ.*, 94, 680–686, doi:10.1016/j.atmosenv.2014.04.053, 2014.
- 920 Marinou, E., Amiridis, V., Biniotoglou, I., Tsikerdekis, A., Solomos, S., Proestakis, E., Konsta, D., Papagiannopoulos, N., Tsekeri, A., Vlastou, G., Zanis, P., Balis, D., Wandinger, U., and Ansmann, A.: Three-dimensional evolution of Saharan dust transport towards Europe based on a 9-year EARLINET-optimized CALIPSO dataset, *Atmos. Chem. Phys.*, 17, 5893–5919, doi:10.5194/acp-17-5893-2017, 2017.
- Mashat, A. W. S., Alamoudi, A. O., Awad, A. M., and Assiri, M. E.: Seasonal variability and synoptic characteristics of dust cases over southwestern Saudi Arabia. *Int. J. Climatol.*, 38, 105-124, doi:10.1002/joc.5164, 2018.
- 925

- Masoom, A., Kosmopoulos, P., Bansal, A., Gkikas, A., Proestakis, E., Kazadzis, S., and Amiridis, V.: Forecasting dust impact on solar energy using remote sensing and modeling techniques, *Sol. Energy*, 228, 317–332, doi:10.1016/j.solener.2021.09.033, 2021.
- Mbourou, G. N., Bertrand, J. J., and Nicholson, S. E.: The diurnal and seasonal cycles of wind-borne dust over Africa north of the Equator, *J. Appl. Meteorol.*, 36, 868–882, doi:10.1175/1520-0450(1997)036<0868:TDASCO>2.0.CO;2, 1997.
- 930 McGill, M., Vaughan, M., Trepte, C., Hart, W., Hlavka, D., Winker, D., and Kuehn, R.: Airborne validation of spatial properties measured by the CALIPSO lidar, *J. Geophys. Res.*, 112, D20201, doi:10.1029/2007JD008768, 2007.
- Mishchenko, M. I. and Travis, L. D.: Satellite retrieval of aerosol properties over the ocean using polarization as well as intensity of reflected sunlight, *J. Geophys. Res.*, 102(D14), 16989–17013, doi:10.1029/96JD02425, 1997a.
- 935 Mishchenko, M. I. and Travis, L. D.: Satellite retrieval of aerosol properties over the ocean using measurements of reflected sun light: Effect of instrumental errors and aerosol absorption, *J. Geophys. Res.*, 102, 13543–13553, doi:10.1029/97JD01124, 1997b.
- Moustaka, A., Korras-Carraca, M. B., Papachristopoulou, K., Stamatis, M., Fountoulakis, I., Kazadzis, S., Proestakis, E., Amiridis, V., Tourpali, K., Georgiou, T., Solomos, S., Spyrou, C., Zerefos, C., and Gkikas, A.: Assessing Lidar Ratio Impact on CALIPSO Retrievals Utilized for the Estimation of Aerosol SW Radiative Effects across North Africa, the Middle East, and Europe. *Remote Sens.*, 16, 1689, doi: 10.3390/rs16101689, 2024.
- 940 Moustaka, A., Korras-Carraca, M.B., Papachristopoulou, K., Fountoulakis, I., Kazadzis, S., Proestakis, E., Amiridis, V., Tourpali, K., Gkikas, A. Assessment of Cloud-Aerosol Lidar with Orthogonal Polarization–Cloud-Aerosol Lidar and Infrared Pathfinder Satellite Observations Retrievals towards Estimating the Aerosol Direct Impact on the Shortwave Radiation Budgets in North Africa, Europe, and the Middle East. *Environ. Sci. Proc.*, 26, 139, doi: 10.3390/envirosciproc2023026139, 2023.
- 945 Moustaka, A., Siomos, N., Kazadzis, S., Proestakis, E., Voudouri, K. A., Lopatin, A., Dubovik, O., Tourpali, K., Zerefos, C., Amiridis, V., and Gkikas, A. (2025): Enhancing dust aerosols monitoring capabilities across North Africa and the Middle East using the A-Train satellite constellation [Data set], Zenodo, doi:10.5281/zenodo.18016524, 2025.
- 950 Müller, D., Ansmann, A., Mattis, I., Tesche, M., Wandinger, U., Althausen, D., and Pisani, G.: Aerosol-type-dependent lidar ratios observed with Raman lidar, *J. Geophys. Res.*, 112, D16202, doi:10.1029/2006JD008292, 2007.
- NASA Langley Research Center: CALIPSO quality statements: lidar level 1B profile products, Version 2.01, NASA, Hampton, VA, USA, 2007.
- 955 Ningombam, S., Larson, E. J. L., Dumka, U. C., Estellés, V., Campanelli, M., and Colwell, S.: Long-term (1995–2018) aerosol optical depth derived using ground based AERONET and SKYNET measurements from aerosol aged-background sites, *Atmos. Pollut. Res.*, 10, 608–620, doi:10.1016/j.apr.2018.10.008, 2019.
- Omar, A. H., Won, J.-G., Winker, D. M., Yoon, S.-C., Dubovik, O., and McCormick, M. P.: Development of global aerosol models using cluster analysis of Aerosol Robotic Network (AERONET) measurements, *J. Geophys. Res.*, 110, D10S14, doi:10.1029/2004JD004874, 2005.

- 960 Omar, A. H., Winker, D. M., Vaughan, M. A., Hu, Y., Trepte, C. R., Ferrare, R. A., Lee, K. P., Hostetler, C. A., Kittaka, C., Rogers, R. R., and Kuehn, R. E.: The CALIPSO Automated Aerosol Classification and Lidar Ratio Selection Algorithm, *J. Atmos. Ocean. Tech.*, 26, 1994–2014, doi:10.1175/2009JTECHA1231.1, 2009.
- Omar, A. H., Winker, D. M., Tackett, J. L., Giles, D. M., Kar, J., Liu, Z., Vaughan, M. A., Powell, K. A., and Trepte, C. R.: CALIOP and AERONET aerosol optical depth comparisons: One size fits none, *Journal of Geophysical Research: Atmospheres*, 118(10), 4748–4766, doi:10.1002/jgrd.50330, 2013.
- 965 U.S. Committee on Extension to the Standard Atmosphere (COESA): *U.S. Standard Atmosphere, 1976*, U.S. Government Printing Office, Washington, D.C., 1976.
- Papachristopoulou, K., Fountoulakis, I., Gkikas, A., Kosmopoulos, P. G., Nastos, P. T., Hatzaki, M., and Kazadzis, S.: 15-Year Analysis of Direct Effects of Total and Dust Aerosols in Solar Radiation/Energy over the Mediterranean Basin, *Remote Sens.-Basel*, 14, 1535, doi:10.3390/rs14071535, 2022.
- 970 Pease, P. P., Tchakerian, V. P., and Tindale, N. W.: Aerosols over the Arabian Sea: geochemistry and source areas for Aeolian desert dust, *J. Arid Environ.*, 39, 477–496, doi:10.1006/jare.1997.0368, 1998.
- Preißler, J., Wagner, F., Pereira, S. N., and Guerrero-Rascado, J. L.: Multi-instrumental observation of an exceptionally strong Saharan dust outbreak over Portugal, *J. Geophys. Res.-Atmos.*, 116, D24204, doi:10.1029/2011JD016527, 2011.
- 975 Proestakis, E., Amiridis, V., Marinou, E., Georgoulas, A. K., Solomos, S., Kazadzis, S., Chimot, J., Che, H., Alexandri, G., Binietoglou, I., Daskalopoulou, V., Kourtidis, K. A., de Leeuw, G., and van der A, R. J.: Nine-year spatial and temporal evolution of desert dust aerosols over South and East Asia as revealed by CALIOP, *Atmos. Chem. Phys.*, 18, 1337–1362, doi:10.5194/acp-18-1337-2018, 2018.
- Prospero, J. M. and Mayol-Bracero, O. L.: Understanding the transport and impact of African dust on the Caribbean basin, *B. Am. Meteorol. Soc.*, 94, 1329–1337, doi:10.1175/BAMS-D-12-00142.1, 2013.
- 980 Raptis, I.-P., Kazadzis, S., Amiridis, V., Gkikas, A., Gerasopoulos, E., and Mihalopoulos, N.: A Decade of Aerosol Optical Properties Measurements over Athens, Greece, *Atmosphere*, 11, 154, doi:10.3390/atmos11020154, 2020.
- Rezazadeh, M., Irannejad, P., and Shao, Y. J. A. R.: Climatology of the Middle East dust events. *Aeolian Research*, 10, 103–109, doi:10.1016/j.aeolia.2013.09.004, 2013.
- 985 Rittmeister, F., Ansmann, A., Engelmann, R., Skupin, A., Baars, H., Kanitz, T., and Kinne, S.: Profiling of Saharan dust from the Caribbean to western Africa – Part 1: Layering structures and optical properties from shipborne polarization/Raman lidar observations, *Atmos. Chem. Phys.*, 17, 12963–12983, doi:10.5194/acp-17-12963-2017, 2017.
- Roccetti, G., Bugliaro, L., Gödde, F., Emde, C., Hamann, U., Manev, M., Sterzik, M. F., and Wehrum, C.: HAMSTER: Hyperspectral Albedo Maps dataset with high Spatial and TEmporal Resolution, *Atmos. Meas. Tech.*, 17, 6025–6046, doi:10.5194/amt-17-6025-2024, 2024.
- 990 Sayer, A. M., Hsu, N. C., Bettenhausen, C., and Jeong, M.-J.: Validation and uncertainty estimates for MODIS Collection 6 “Deep Blue” aerosol data, *J. Geophys. Res. Atmos.*, 118, 7864–7872, doi:10.1002/jgrd.50600, 2013.

- Sayer, A. M., Smirnov, A., Hsu, N. C., and Holben, B. N.: A pure marine aerosol model, for use in remote sensing applications, *J. Geophys. Res.*, 117, D05213, doi:10.1029/2011JD016689, 2012.
- 995 Schepanski, K.: Transport of Mineral Dust and Its Impact on Climate, *Geosciences*, 8, 151, doi:10.3390/geosciences8050151, 2018.
- Scheuvens, D., Schütz, L., Kandler, K., Ebert, M., and Weinbruch, S.: Bulk composition of northern African dust and its source sediments— A compilation, *Earth-Sci. Rev.*, 116, 170194, doi:10.1016/j.earscirev.2012.08.005, 2013.
- Schuster, G. L., Vaughan, M., MacDonnell, D., Su, W., Winker, D., Dubovik, O., Lapyonok, T., and Trepte, C.: Comparison
1000 of CALIPSO aerosol optical depth retrievals to AERONET measurements, and a climatology for the lidar ratio of dust, *Atmos. Chem. Phys.*, 12, 7431–7452, doi:10.5194/acp-12-7431-2012, 2012.
- Schuster, G. L., Dubovik, O., and Arola, A.: Remote sensing of soot carbon – Part 1: Distinguishing different absorbing aerosol species, *Atmos. Chem. Phys.*, 16, 1565–1585, doi:10.5194/acp-16-1565-2016, 2016.
- Shi, Y., Zhang, J., Reid, J. S., Holben, B., Hyer, E. J., and Curtis, C.: An analysis of the collection 5 MODIS over-ocean
1005 aerosol optical depth product for its implication in aerosol assimilation, *Atmos. Chem. Phys.*, 11, 557–565, doi:10.5194/acp-11-557-2011, 2011.
- Sinyuk, A., Holben, B. N., Eck, T. F., Giles, D. M., Slutsker, I., Korokin, S., Schafer, J. S., Smirnov, A., Sorokin, M., and Lyapustin, A.: The AERONET Version 3 aerosol retrieval algorithm, associated uncertainties and comparisons to Version 2, *Atmos. Meas. Tech.*, 13, 3375–3411, doi:10.5194/amt-13-3375-2020, 2020.
- 1010 Solmon, F., Nair, V. S., and Mallet, M.: Increasing Arabian dust activity and the Indian summer monsoon, *Atmos. Chem. Phys.*, 15, 8051–8064, doi:10.5194/acp-15-8051-2015, 2015.
- Steinmetz, F., Ramon, D., Deschamps, P. Y., and Nicolas, J. M.: Analysis of the first ocean color products from POLDER 3 onboard PARASOL. In *Remote Sensing of the Ocean, Sea Ice, and Large Water Regions 2005*, 5977, 209–217, doi:10.1117/12.629878, 2005.
- 1015 Szczepanik, D. M., Stachlewska, I. S., Tetoni, E., and Althausen, D.: Properties of Saharan Dust Versus Local Urban Dust— A Case Study, *Earth and Space Sc.*, 8, e2021EA001816, doi:10.1029/2021EA001816, 2021.
- Tackett, J. L., Winker, D. M., Getzewich, B. J., Vaughan, M. A., Young, S. A., and Kar, J.: CALIPSO lidar level 3 aerosol profile product: version 3 algorithm design, *Atmos. Meas. Tech.*, 11, 4129–4152, doi:10.5194/amt-11-4129-2018, 2018.
- Tackett, J. L., Kar, J., Vaughan, M. A., Getzewich, B. J., Kim, M.-H., Vernier, J.-P., Omar, A. H., Magill, B. E., Pitts, M. C.,
1020 and Winker, D. M.: The CALIPSO version 4.5 stratospheric aerosol subtyping algorithm, *Atmos. Meas. Tech.*, 16, 745–768, doi:10.5194/amt-16-745-2023, 2023.
- Tesche, M., Ansmann, A., Müller, D., Althausen, D., Mattis, I., Heese, B., Freudenthaler, V., Wiegner, M., Esselborn, M., Pisani, G., and Knippertz, P.: Vertical profiling of Saharan dust with Raman lidars and airborne HSRL in southern Morocco during SAMUM, *Tellus B*, 61, 144–164, doi:10.1111/j.16000889.2008.00390.x, 2009.

- 1025 Tesche, M., Groß, S., Ansmann, A., Müller, D., Althausen, D., Freudenthaler, V., and Esselborn, M.: Profiling of Saharan dust and biomass-burning smoke with multiwavelength polarization Raman lidar at Cape Verde, *Tellus B*, 63, 16360, doi:10.3402/tellusb.v63i4.16360, 2011.
- Textor, C., Schulz, M., Guibert, S., Kinne, S., Balkanski, Y., Bauer, S., Berntsen, T., Berglen, T., Boucher, O., Chin, M., Dentener, F., Diehl, T., Easter, R., Feichter, H., Fillmore, D., Ghan, S., Ginoux, P., Gong, S., Grini, A., Hendricks, J., Horowitz, L., Huang, P., Isaksen, I., Iversen, I., Kloster, S., Koch, D., Kirkevåg, A., Krist jansson, J. E., Krol, M., Lauer, A., Lamarque, J. F., Liu, X., Mon tanaro, V., Myhre, G., Penner, J., Pitari, G., Reddy, S., Seland, Ø., Stier, P., Takemura, T., and Tie, X.: Analysis and quantification of the diversities of aerosol life cycles within AeroCom, *Atmos. Chem. Phys.*, 6, 1777–1813, doi:10.5194/acp-6-1777-2006, 2006.
- 1030 Tindan, J. Z., Jin, Q., and Pu, B.: Understanding day–night differences in dust aerosols over the dust belt of North Africa, the Middle East, and Asia, *Atmos. Chem. Phys.*, 23, 5435–5466, doi:10.5194/acp-23-5435-2023, 2023.
- Urbanneck, C.: Retrieval of aerosol optical and microphysical properties in Cyprus during A-LIFE and CyCARE by lidar and closure studies with airborne insitu measurements– Towards aerosol-cloud interaction investigations, MSc thesis, Leipzig University, https://www.tropos.de/fileadmin/user_upload/Institut/Abteilungen/Fernerkundung/Daten_PDF/MA_claudia_urbanneck.pdf, (last access: 25 November 2024), 2018.
- 1040 Wandinger, U., Ansmann, A., Reichardt, J., and Deshler, T.: Determination of stratospheric aerosol microphysical properties from independent extinction and backscattering measurements with a Raman lidar, *Appl. Optics*, 34, 8315, doi:10.1364/AO.34.008315, 1995.
- Wandinger, U., Floutsi, A. A., Baars, H., Haarig, M., Ansmann, A., Hünerbein, A., Docter, N., Donovan, D., van Zadelhoff, G.-J., Mason, S., and Cole, J.: HETEAC – the Hybrid End-To-End Aerosol Classification model for EarthCARE, *Atmos. Meas. Tech.*, 16, 2485–2510, doi:10.5194/amt-16-2485-2023, 2023.
- 1045 Wandinger U., Hiebsch, A., Mattis, I., Pappalardo, G., Mona, L., and Madonna, F.: Aerosols and Clouds: Long-term Database from Spaceborne Lidar Measurements, Executive Summary, available at: <http://esamultimedia.esa.int/docs/gsp/C21487ExS.pdf> (last access: 10 November 2024), ESTEC Contract 21487/08/NL/HE, 2011.
- 1050 Warren, A., Chappell, A., Todd, M. C., Bristow, C., Drake, N., Engelstaedter, S., Martins, V., M’Bainayel, S., and Washington, R.: Dust-raising in the dustiest place on earth, *Geomorphology*, 92, 25–37, doi:10.1016/j.geomorph.2007.02.007, 2007.
- Washington, R., Bouet, C., Cautenet, G., Mackenzie, E., Ashpole, I., Engelstaedter, S., Lizcano, G., Henderson, G. M., Schepanski, K., and Tegen, I.: Dust as a tipping element: The Bodele Depression, Chad, *P. Natl. Acad. Sci. USA*, 106, 20564–20571, doi:10.1073/pnas.0711850106, 2009.
- 1055 Wehr, T., Kubota, T., Tzeremes, G., Wallace, K., Nakatsuka, H., Ohno, Y., Koopman, R., Rusli, S., Kikuchi, M., Eisinger, M., Tanaka, T., Taga, M., Deghaye, P., Tomita, E., and Bernaerts, D.: The EarthCARE mission – science and system overview, *Atmos. Meas. Tech.*, 16, 3581–3608, doi:10.5194/amt-16-3581-2023, 2023.

- Weinzierl, B., Ansmann, A., Prospero, J., Althausen, D., Benker, N., Chouza, F., Dollner, M., Farrell, D., Fomba, W., Freudenthaler, V., Gasteiger, J., Groß, S., Haarrig, M., Heinold, B., Kandler, K., Kristensen, T., Mayol-Bracero, O., Müller, T.,
1060 Reitebuch, O., Sauer, D., Schäfler, A., Schepanski, K., Spanu, A., Tegen, I., Toledano, C., and Walser, A.: The Saharan Aerosol Long-range Transport and Aerosol-Cloud Interaction Experiment (SALTRACE): overview and selected highlights, *B. Am. Meteorol. Soc.*, 98, 1427–1451, doi:10.1175/BAMS-D-15-00142.1, 2017.
- Winker, D. M., Vaughan, M. A., Omar, A., Hu, Y., Powell, K. A., Liu, Z., Hunt, W. H., and Young, S. A.: Overview of the CALIPSO mission and CALIOP data processing algorithms, *J. Atmos. Ocean. Tech.*, 26, 2310–2323,
1065 doi:10.1175/2009JTECHA1281.1, 2009.
- Winker, D. M., Pelon, J., Coakley Jr, J. A., Ackerman, S. A., Charlson, R. J., Colarco, P. R., Flamant, P., Fu, Q., Hoff, R. M., Kittaka, C., Kubar, T. L., Le Treut, H., McCormick, M. P., Mégie, G., Poole, L., Powell, K., Treppe, C., Vaughan, M. A., and Wielicki, B. A.: The CALIPSO mission: A global 3D view of aerosols and clouds, *Bull. Amer. Meteor. Soc.*, 91, 1211–1229, doi:10.1175/2010BAMS3009.1, 2010.
- 1070 Winker, D. M., Tackett, J. L., Getzewich, B. J., Liu, Z., Vaughan, M. A., and Rogers, R. R.: The global 3-D distribution of tropospheric aerosols as characterized by CALIOP, *Atmospheric Chemistry and Physics*, 13(6), 3345–3361, doi:10.5194/acp-13-3345-2013, 2013.
- Wang, Z., Shi, C., Zhang, H., Chen, Y., Chi, X., Xia, C., Wang, S., Zhu, Y., Zhang, K., Chen, X., Xing, C., and Liu, C.: Measurement report: Dust and anthropogenic aerosols' vertical distributions over northern China dense aerosols gathered at
1075 the top of the mixing layer, *Atmos. Chem. Phys.*, 23, 14271–14292, doi:10.5194/acp-23-14271-2023, 2023.
- Xiong, J., Zhao, T., Bai, Y., Liu, Y., Han, Y., and Guo, C.: Climate characteristics of dust aerosol and its transport in major global dust source regions. *Journal of Atmospheric and Solar-Terrestrial Physics*, 209, 105415, doi: 10.1016/j.jastp.2020.105415, 2020.
- Yu, Y., Notaro, M., Liu, Z., Kalashnikova, O., Alkolibi, F., Fadda, E., and Bakhrjy, F.: Assessing temporal and spatial
1080 variations in atmospheric dust over Saudi Arabia through satellite, radiometric, and station data, *J. Geophys. Res.-Atmos.*, 118, 13-253, doi:10.1002/2013JD020677, 2013.
- Yu, Y., Notaro, M., Liu, Z., Wang, F., Alkolibi, F., Fadda, E., and Bakhrjy, F.: Climatic controls on the interannual to decadal variability in Saudi Arabian dust activity: toward the development of a seasonal dust prediction model, *J. Geophys. Res.-Atmos.*, 120, 1739–1758, doi:10.1002/2014JD022611, 2015.
- 1085 Yu, X., Nichol, J., Lee, K.H., Li, J., and Wong, M.S.: Analysis of long-term aerosol optical properties combining AERONET sunphotometer and satellite-based observations in Hong Kong. *Remote Sens.*, 14, 5220, doi:10.3390/rs14205220, 2022.
- Zender, C. S., Miller, R. L. R. L., and Tegen, I.: Quantifying mineral dust mass budgets: Terminology, constraints, and current estimates, *Eos, Trans. Am. Geophys. Union*, 85(48), 509–512, doi:10.1029/2004EO480002, 2004.
- Zhang, J. and Reid, J. S.: MODIS aerosol product analysis for data assimilation: Assessment of over-ocean level 2 aerosol
1090 optical thickness retrievals, *J. Geophys. Res.-Atmos.*, 111, D22207, doi:10.1029/2005JD006898, 2006.

Zhang, T., Zheng, M., Sun, X., Chen, H., Wang, Y., Fan, X., Pan, Y., Quan, J., Liu, J., Wang, Y., Lyu, D., Chen, S., Zhu, T., and Chai, F.: Environmental impacts of three Asian dust events in the northern China and the northwestern Pacific in spring 2021, *Sci. Total Environ.*, 859, 160230, doi:10.1016/j.scitotenv.2022.160230, 2023.

1095 Zhang, X., Li, L., Chen, C., Chen, X., Dubovik, O., Derimian, Y., Gui, K., Zheng, Y., Zhao, H., Zhang, L., Guo, B., Wang, Y., Holben, B., Che, H., and Zhang, X.: Validation of the aerosol optical property products derived by the GRASP/Component approach from multi-angular polarimetric observations, *Atmos. Res.*, 263, 105802, doi:10.1016/j.atmosres.2021.105802, 2021.

1100 Zhang, X., Li, L., Chen, C., Zheng, Y., Dubovik, O., Derimian, Y., Lopatin, A., Gui, K., Wang, Y., Zhao, H., Liang, Y., Holben, B., Che, H., and Zhang, X.: Extensive characterization of aerosol optical properties and chemical component concentrations: Application of the GRASP/Component approach to long-term AERONET measurements, *Sci. Total Environ.*, 812, 152553, doi:10.1016/j.scitotenv.2021.152553, 2022.